Turbulent mixing of a passive scalar

Mark Holzer and Eric D. Siggia
Laboratory of Atomic and Solid State Physics, Cornell University, Ithaca, New York 14853-2501

The statistically stationary state of a turbulently advected passive scalar is studied, with an imposed linear mean gradient in two dimensions, via a number of numerical experiments. For a synthetic Gaussian velocity field, which is generated by a linear stochastic process, and whose spectra and Eulerian correlation time follow Kolmogorov scaling on all scales, the exponents of the scalar spectra are consistent with 5/3 or 17/3 depending on the diffusivity. For large Péclet numbers (Pe), the probability density function (PDF) of the scalar gradients perpendicular to the mean is well fit, from about 0.1–10 times the root-mean-square value, by a stretched exponential with exponent ~0.6. The PDF for gradients parallel to the mean has similar tails and a $\mathcal{O}(1)$ skewness for all Pe studied. The scalar has a ramp-and-cliff structure similar to that first seen in shear-flow experiments with scalars. A physical picture of the mechanism by which the ramp-and-cliff features form is given. A second model with the velocity evolving under the Euler equations restricted to a band of wave numbers produces the k^{-1} Batchelor spectrum when the scalar is dissipated with a hyperdiffusivity ($\propto k^4$). For physical dissipation ($\propto k^2$), the PDF of the scalar has exponential tails, and for gradients less than the cutoff set by the maximum strain, the PDF of the gradients is similar to that obtained with the stochastic velocity model. The PDF of the dissipation is approximately stretched exponential like the gradient PDFs and not lognormal. The skewness of the gradients parallel to the mean decreases with decreasing autocorrelation time of the velocity, and the gradient PDFs assume a limiting form in the white-noise limit.

I. INTRODUCTION

Soon after Kolmogorov's first seminal papers[1] on the energy spectrum of turbulence, cascade ideas were applied to passive scalars advected by turbulence.[2] Several decades of increasingly detailed experiments with scalars (e.g., Refs. 3–12) have clearly shown significant deviations from theoretical predictions, yet in themselves have not been comprehensive enough to point to a refined theory. The numerical experiments presented in this article aim to further dissect turbulent mixing. Although we drastically simplify the problem by utilizing synthetic velocity fields and periodic boundary conditions, we find, within our limited range of scales, the same conflicts with cascade ideas that are observed in natural flows.

Experiments have shown the scalar to "misbehave" in a number of ways. Its wave-number spectrum can be fit very well to a power law over a range of about 30 in wave number at moderate Re, but the exponent can vary from 1.3 to 1.6 depending on the large-scale geometry.[11,12] At higher Re, some experiments[11] suggest the exponent tends to 5/3, but only a single geometry was examined. Also, the second-order temperature structure function in the boundary layer shows two power-law regimes with a pronounced break in the exponent.[5] For very large Prandtl (or Schmidt) number, experiments[6–8] have failed to clearly discern Batchelor's k^{-1} regime which is generally felt to be a solid theoretical result.[13] Finally, we note that the scalar derivative kurtosis can be quite large (~10–50) (Refs. 3 and 4), but its systematic dependence on Re is not available. By this measure, the scalar is more intermittent than the velocity.

Although the variability of the spectral exponent seen in experiments might be an artifact of moderate Re, the scalar derivative skewness is of order 0.8 and shows no signs of decreasing with Re for the highest Re attainable in the laboratory[3–5,11] A Re-independent derivative skewness contradicts cascade ideas, which predict that the relative anisotropy on a wave-number scale k is $s_L/(\epsilon_v k^2)^{1/3}$, where s_L is the large-scale strain and ϵ_v is the usual kinetic-energy dissipation rate. In addition, inspection of time series of the scalar, $\Theta(t)$, suggests that the events responsible for the skewness involve scalar differences of the order of the total variation ($\sim \sqrt{\langle\Theta^2\rangle}$) over scales of order the Taylor microscale.[4,14]

The anomalous behavior of the derivative skewness was first noticed for the temperature field, Θ, in a turbulent boundary layer.[3,4] This is a complicated flow whose only purpose, from the point of view of symmetry (and apart from its intrinsic interest), is to convert the mean scalar gradient normal to the heated plate, $\partial\langle\Theta\rangle/\partial y$, into a streamwise gradient, $\partial\Theta/\partial x$, which is more easily measured, i.e., by symmetry,

$$\text{sign}\left\langle\left(\frac{\partial\Theta}{\partial x}\right)^3\right\rangle = -\text{sign}\left[\left(\frac{\partial\langle u\rangle}{\partial y}\right)\left(\frac{\partial\langle\Theta\rangle}{\partial y}\right)\right] \qquad (1)$$

(both sides are odd under $x \to -x$, and even under $y \to -y$). A boundary layer is inhomogeneous in y and scalar gradients are maintained in part by direct injection from the wall, rather than by degradation of larger scales. Cascade ideas still assert local isotropy far from the walls.

The purpose of this paper is to sharpen the conflict with cascade ideas by examining the scalar under much simpler conditions for which the flow is precisely homoge-

neous and isotropic. To break the rotational invariance of the scalar on the large scales, so that the derivative skewness does not vanish by symmetry [in fact, we find it remains $\mathcal{O}(1)$], we impose a constant mean gradient, **g**, on the scalar, i.e., $\Theta(\mathbf{x}) = \theta(\mathbf{x}) + \mathbf{g} \cdot \mathbf{x}$. The scalar transport equation for the fluctuation, θ, then reads

$$\partial_t \theta + \mathbf{v} \cdot \nabla \theta = \kappa \nabla^2 \theta - \mathbf{v} \cdot \mathbf{g}, \tag{2}$$

where κ is the scalar diffusivity, and **v** is an incompressible ($\nabla \cdot \mathbf{v} = 0$) velocity field with a dynamics of its own and homogeneous-isotropic statistics. The term $\mathbf{v} \cdot \mathbf{g}$ is seen to act as a spatially homogeneous source of scalar fluctuations, which maintains a nontrivial statistically stationary state. For simplicity we take both $\mathbf{v}(\mathbf{x})$ and $\theta(\mathbf{x})$ to have periodic boundary conditions. When necessary, any artifacts due to the periodicity can be eliminated by choosing the integral scale of the velocity to be much less than the box size. To further simplify the problem, and for reasons of computational efficiency, we will only work in two dimensions. Although the cascade regimes of the velocity vary greatly between two and three dimensions, those for the scalar do not when a comparable velocity is imposed, since the conservation properties of the scalar do not depend on dimensionality. We shall employ two-dimensional (2-D) model velocity fields which mimic three-dimensional (3-D) turbulence in various regimes by having appropriate spatial and frequency spectra. For technical simplicity, we will take the multivariate (equal-time) probability density function (PDF) of the velocity to be Gaussian, because we do not think that the velocity skewness matters and too little is known about intermittency to model it with confidence. Furthermore, the PDF of the velocity at a point is very nearly Gaussian in experiments.[15,16] An obvious pathology of two dimensions, that with a static velocity field closed streamlines prevent convective transport, is not an issue if the velocity is time dependent on a reasonable scale.

It is our goal to demonstrate that even with a Gaussian, homogeneous, isotropic velocity field, the statistically stationary state of Eq. (2) reproduces many of the anomalous features of turbulent transport seen experimentally in more complex settings. To that end, we will primarily be interested in spatial spectra, and the scalar and scalar-gradient PDFs whose character and dependence on the dimensionless parameters we will determine within our computational limits. What emerges can be examined in sufficient detail to suggest the first steps toward a phenomenological theory.

The problem we have posed could be addressed in the laboratory with either grid or continuously forced turbulence by measuring the temperature derivative along an imposed linear temperature gradient (under conditions where the temperature is passive). However, this has not been done yet, although the scalar itself has been studied under those conditions.[9,10]

In the following section we recapitulate the pertinent cascade theories. In Sec. III we describe the two model velocity fields which we use to advect the scalar. Numerical results for spectra, scalar, and scalar-derivative PDFs

for the two models comprise Secs. IV and V. The conclusion reconsiders the anomalous features of turbulent mixing based on our simulations.

II. SUMMARY OF RELEVANT THEORY

The spectra $E(k)$ are normalized so that for the scalar $\langle \theta^2(\mathbf{x}) \rangle \equiv \int_0^\infty dk\, E_\theta(k)$, and for the velocity $\langle \mathbf{v}^2(\mathbf{x}) \rangle / 2 \equiv \int_0^\infty dk\, E_v(k)$. The turbulent velocity field is characterized by an integral scale, L, the mean kinetic energy dissipation rate, ϵ_v, and the dissipation, or Kolmogorov, scale, $l_v = (\nu^3/\epsilon_v)^{1/4}$, where ν is the kinematic viscosity. Correspondingly, the scalar is characterized by a mean dissipation rate of scalar variance, ϵ_θ, and a dissipation scale, l_θ. The $\langle \theta \theta v \rangle$ triple correlation obeys a von Kármán–Howarth-type relation,[17] which, for the stationary state, is given by

$$\frac{1}{4} \frac{\partial}{\partial r_l} \langle [\Delta\theta(\mathbf{r})]^2 \Delta v_i(\mathbf{r}) \rangle$$
$$= \mathbf{g} \cdot \langle \theta(\mathbf{x}) \mathbf{v}(\mathbf{x}') \rangle - \kappa \frac{\partial^2}{\partial \mathbf{x}^2} \langle \theta(\mathbf{x}) \theta(\mathbf{x}') \rangle, \tag{3}$$

where $\mathbf{r} \equiv \mathbf{x} - \mathbf{x}'$, $\Delta\theta(\mathbf{r}) \equiv \theta(\mathbf{x}) - \theta(\mathbf{x}')$, and $\Delta\mathbf{v}(\mathbf{r}) \equiv \mathbf{v}(\mathbf{x}) - \mathbf{v}(\mathbf{x}')$. For scales r such that $L \gg r \gg l_\theta$, the dissipation term in (3) is negligible, and $\mathbf{g} \cdot \langle \theta(\mathbf{x}) \mathbf{v}(\mathbf{x}') \rangle = \mathbf{g} \cdot \langle \theta(\mathbf{x}) \mathbf{v}(\mathbf{x}) \rangle + \mathcal{O}(r/L)$, with $\mathbf{g} \cdot \langle \theta(\mathbf{x}) \mathbf{v}(\mathbf{x}) \rangle = -\epsilon_\theta/2$, since in the stationary state we have the balance [$\mathbf{x} = \mathbf{x}'$ in Eq. (3), plus the identity $\nabla \cdot \langle \theta \nabla \theta \rangle \equiv 0$]

$$-\mathbf{g} \cdot \langle \theta(\mathbf{x}) \mathbf{v}(\mathbf{x}) \rangle = \kappa \langle \nabla\theta \cdot \nabla\theta \rangle \equiv \epsilon_\theta/2. \tag{4}$$

Assuming scaling for the correlations, the r dependence of $\Delta\theta(r)$, and hence the spectrum, follow immediately. Thus, if $\mathbf{v}(\mathbf{x})$ has a Kolmogorov spectrum, one derives from (3) the Oboukhov–Corrsin result,[2]

$$E_\theta(k) \propto \epsilon_\theta \epsilon_v^{-1/3} k^{-5/3}, \tag{5}$$

for $L^{-1} \ll k \ll \min(l_\theta^{-1}, l_v^{-1})$, where the dissipation scale, l_θ, (the Corrsin scale) is given by

$$l_\theta = \left(\frac{\kappa^3}{\epsilon_v} \right)^{1/4} = \mathrm{Pr}^{-3/4} l_v, \tag{6}$$

where $\mathrm{Pr} \equiv \nu/\kappa$ is the Prandtl (or Schmidt) number.

For small Pr, $l_\theta \gg l_v$, the scalar dissipation is still concentrated at l_θ, but a second steeper power law extends beyond the scalar-inertial regime (5), in which the scalar at $l_\theta^{-1} \ll k \ll l_v^{-1}$ is maintained via a nonlocal cascade by beating the velocity Fourier modes, $\mathbf{v}(\mathbf{k})$, against $\theta(\mathbf{q})$, for $q \sim l_\theta^{-1}$. Thus, factoring the velocity out of the advection-diffusion balance[18]

$$\int d\mathbf{q}\, d\mathbf{q}' \langle \mathbf{v}(\mathbf{k}-\mathbf{q}) \cdot \mathbf{q} \theta(\mathbf{q}) \mathbf{v}(-\mathbf{k}+\mathbf{q}') \cdot \mathbf{q}' \theta(-\mathbf{q}') \rangle$$
$$= \kappa^2 k^4 \langle \theta(\mathbf{k}) \theta(-\mathbf{k}) \rangle, \tag{7}$$

since the integral is dominated by $q, q' \ll k$, we obtain the Batchelor–Howell–Townsend[19] result

$$E_\theta(k) \propto \epsilon_\theta \kappa^{-3} k^{-4} E_v(k), \tag{8}$$

which for a Kolmogorov velocity is $\propto k^{-17/3}$.

M. Holzer and E. D. Siggia   1821

In the opposite limit, $l_v \gg l_\theta$, and for $l_v^{-1} \ll k \ll l_\theta^{-1}$, the velocity field can in effect be replaced by a random strain field of amplitude $s \sim (\epsilon_v/\nu)^{1/2}$. Batchelor[13,20] then showed that the scalar is randomly folded, or in terms of the spectrum that

$$E_\theta(k) \propto (\epsilon_\theta/s)k^{-1}. \qquad (9)$$

In the Batchelor regime, the dissipation scale is determined by balancing diffusion against the compressive effect of the strain, i.e.,

$$l_\theta \equiv \left(\frac{\kappa}{s}\right)^{1/2} = \text{Pr}^{-1/2} l_v. \qquad (10)$$

For $l_v \gg r \gg l_\theta$, Eqs. (9) and (10) imply that $\langle(\Delta\theta)^2\rangle \sim (\epsilon_\theta/s)\log(r/l_\theta)$, which, except for the logarithm that cannot be extracted from scaling, also follows from (3) since $\Delta v \sim sr$, for $r \gg l_v$. It should be emphasized that only random strain and large Péclet number are required for (9) and (10). *There is no need for large Reynolds number.*

The scalar PDF is dominated by the integral scales. Under conditions of an imposed mean gradient as in (2), a phenomenological theory predicted there to be exponential tails[21] that were subsequently seen experimentally.[9,10] A coarse-grained model[22] replaces turbulent advection by random, instantaneous interchanges of fluid particles separated by an integral scale. In this model, the tails of the PDF result from a burst of interchange events which occur with Poisson-distributed probability. A calculation that remains more faithful to the continuum equations finds tails in the scalar PDF from transient suppression of the strain-enhanced mixing along a Lagrangian trajectory.[23] Nearly exponential (but transient) scalar PDFs were also seen in direct numerical simulations of 3-D turbulence.[24]

A heuristic mechanism for the scalar derivative skewness was recently proposed in a slightly different context:[25] Since Eq. (4) shows that the correlation $\mathbf{g} \cdot \langle \mathbf{v}\theta \rangle$ is negative, positive (negative) fluctuations of the scalar, which are coherent on the integral scale (scalar "blobs"), are more likely to be moving against (with) the gradient. One may then expect that such blobs develop a ramp-like profile with a steepening leading edge and a flattening "wake."

Our simulations in Sec. IV, however, suggest an alternative mechanism for the production of ramps, which seems to us more generic and was also seen in experiments on a planar jet.[26] The presence of ramps immediately implies a nonzero derivative skewness. In sharp contradiction with notions of eddy diffusivity, both experimental data[4] and our simulations show that the thickness of the leading edge of the ramps scales with the molecular diffusivity, κ, even for the highest Péclet numbers studied.

It is useful to have some quantitative estimate for the skewness based on mixing-length or eddy-diffusion ideas so as to have an objective way of deciding what is "anomalous." The most straightforward procedure would estimate $\langle(\hat{\mathbf{g}} \cdot \nabla\theta)^3\rangle$ as $|\mathbf{g}|^3$, since only the large scales have a mean gradient. The denominator of the skewness is rigorously expressed as $\propto (\epsilon_\theta/\kappa)^{3/2}$. Thus, writing ϵ_θ in terms of large-scale quantities [cf. Eq. (4)], one would conclude

that the derivative skewness goes to zero with increasing Pe as $\text{Pe}^{-3/2}$.[27] [We shall always define the skewness for the periodic part of the scalar, θ, which appears in Eq. (2). For the full scalar field, Θ, the above reasoning leads to a $\text{Pe}^{-1/2}$ dependence.]

There are no theoretical predictions for the scalar-gradient PDFs except in the Batchelor regime (9), where it is lognormal under some circumstances.[28] We do expect that the gradient will not exceed $\tilde{\theta}\sqrt{s/\kappa}$, where s is the maximum sustained strain and $\tilde{\theta}$ is a temperature difference which is itself exponentially distributed.[23]

III. NUMERICAL MODELS FOR THE ADVECTING VELOCITY

A simple way to mimic in 2D the random flow of 3-D turbulence in its inertial range is to give the Fourier modes of the streamfunction, ψ_k, the stochastic dynamics

$$\partial_t \psi_k(t) = -\gamma(k)\psi_k(t) + \eta_k(t), \qquad (11)$$

where $\eta_k(t)$ is a white-noise process with statistically independent real and imaginary parts. Because we want the velocity field to be homogeneous and isotropic, we take

$$\langle \eta_k(t)\eta_{k'}(t')\rangle = 2\sigma^2(k)\delta(t-t')\delta_{k,-k'}. \qquad (12)$$

Since the stochastic forcing is Gaussian, and Eq. (11) is linear, ψ_k is itself a stationary Gaussian process with correlations

$$\langle \psi_k(t)\psi_{k'}(t')\rangle = \delta_{k,-k'}\frac{\sigma^2(k)}{\gamma(k)}e^{-\gamma(k)|t-t'|}, \qquad (13)$$

also known as an Ornstein–Uhlenbeck (OU) process.[29] We obtain the desired Kolmogorov scalings of $E_v(k) \sim k^{-5/3}$ and $\gamma(k) \sim k^{2/3}$ with $\sigma(k) \propto k^{-2}$.

Clearly model (11), while having the correct spectrum, is not free of physical pathologies. Since (11) is a linear process, "eddies" are not self-advecting and hence the model is not Galilean invariant so that we cannot define a proper Lagrangian frequency for the velocity. We merely take the Eulerian frequency, $\gamma(k)$, to scale like the Lagrangian frequency as predicted by Kolmogorov. We choose the free time scale in $\gamma(k)$ such that for an integral scale L and integral time $T \equiv L/\sqrt{\langle \mathbf{v}^2\rangle}$, $\gamma(2\pi/L) = 1/T$.

Large-scale velocities, $V \sim L/T$, sweep the scalar *past* spatial velocity structures of wavelength $k^{-1} \ll L$, so that scalar fluctuations see a change in the velocity at the sweeping frequency $\tau_s^{-1} \sim Vk = (Lk)/T$, which is clearly faster than $\gamma(k) \sim (1/T)(Lk)^{2/3}$. This lessens the eddy diffusivity, $\kappa_e(r)$, experienced by the scalar on scale r, which following Taylor,[30] we estimate as

$$\kappa_e(r) = \langle[\Delta v(r)]^2\rangle\tau_s \sim VL(r/L)^{5/3}, \qquad (14)$$

rather than $\kappa_e(r) \sim VL(r/L)^{4/3}$, which follows from Kolmogorov scaling. In Sec. IV we study the sensitivity of the model to the choice of time scale, $\gamma^{-1}(2\pi/L)$, and find that the suppression of eddy diffusivity is not a serious deficiency of the model.

The sweep-enhanced diffusivity (14) also prevents us from simply deducing the Oboukhov–Corrsin result (5) by

factoring the von Kármán–Howarth relation (3). Instead, since the correlation time is reduced, we can work in the white-noise limit and adapt a Richardson-like closure[13] which, neglecting indices, reads

$$\frac{\partial}{\partial r}\left(\kappa_e(r) \frac{\partial}{\partial r} \langle (\Delta\theta)^2 \rangle \right) \sim \epsilon_\theta. \tag{15}$$

Hence, $\langle (\Delta\theta)^2 \rangle \sim r^{1/3}$, or $E_\theta(k) \sim k^{-4/3}$. Actually, our numerical exponent is much closer to 5/3 than to 4/3, which may reflect naturally occurring numerical factors that push the crossover between (14) and the Kolmogorov result to smaller scales than we can resolve. In any event, as already noted, laboratory experiments give exponents of the scalar spectrum in the range of 4/3–5/3, so that our "incorrect" exponent in itself is not a significant limitation of the model.

In order to avoid the pathologies of the OU velocity, we also consider the case of inviscid 2-D Euler flow with wave numbers restricted to a band, i.e.,

$$\partial_t \omega + \mathscr{A}(\mathbf{v} \cdot \nabla \omega) = 0, \tag{16}$$

where $\omega(\mathbf{x}) = \hat{\mathbf{z}} \cdot \nabla \times \mathbf{v}(\mathbf{x})$ is the vorticity, whose Fourier modes we restrict to lie in an annular region, or "band," in k space defined by $k_{min} < k < k_{max}$. In order for the dynamics to preserve this restriction on the velocity, we introduced the projection operator $\mathscr{A}$ in (16) which zeros all modes not in the prescribed band. This restricted Euler dynamics is easily shown to conserve both kinetic energy and enstrophy. Furthermore, the dynamics (16) can be shown to obey a Liouville theorem (i.e., to conserve phase-space area), which together with an ergodicity hypothesis, implies a stationary canonical Boltzmann ensemble,[31] $\sim \exp[- \Sigma_k (\alpha + \beta k^2) \mathbf{v}_k \cdot \mathbf{v}_{-k}]$, for arbitrary α, β. An equal-time, one-point Gaussian PDF for the velocity follows immediately.

Model (16) has the advantage of being self-advecting and hence it contains no free time scale. However, the model is not capable of mimicking a 3-D inertial range. In fact, because of the quadratic invariants and the Boltzmann ensemble, the velocity has an equipartition equilib-

rium spectrum[32] of the form $E_v(k) \propto k(k_0^2 + k^2)^{-1}$. Therefore, we shall use this model only when the wave-number band is narrow, i.e., $k_{max}/k_{min} \lesssim 2$, which we may view as a turbulent velocity field that has been coarse grained to the integral scale.[22] The same model is also useful to explore the Batchelor regime, i.e., to examine the structure of the scalar for $k > k_{max}$.

Briefly, these velocity models for scalar advection were implemented as follows. The numerics are performed on a $N \times N$ grid with physical dimensions $2\pi \times 2\pi$ giving a wave-number spacing of unity. The linear terms in the equations of motion (for both streamfunction and scalar) are treated implicitly and time stepping is done in Fourier space with a second-order Runge–Kutta scheme. All convolutions are fully dealiased using the algorithm of Ref. 33. The models are typically initialized with a Gaussian-random velocity field of the appropriate spectrum, and with $\theta(\mathbf{x}) = 0$. For all runs with the restricted Euler model, we have initialized the velocity with an equilibrium spectrum truncated at k_{min} and k_{max} and peaked at $k_0 = (k_{max} + k_{min})/2$. Statistical stationarity is typically achieved after ~ 5–10 integral times as ascertained by monitoring the instantaneous, spatially averaged scalar variance and dissipation.

IV. RESULTS FOR KOLMOGOROV–ORNSTEIN-UHLENBECK ADVECTION

We use the OU stochastic model of the velocity, with a $k^{-5/3}$ spectrum for *all* resolved wave numbers, to investigate the case $l_\theta > l_v$, or equivalently, the case of small Pr. In order to improve the statistics which fluctuate with the integral scales, we only allow velocity modes with $k \geqslant 2$, which gives us four integral volumes with integral scale $L = \pi$. We define a Péclet number, $Pe \equiv VL/\kappa$, with $V \equiv \sqrt{\langle |\mathbf{v}(\mathbf{x})|^2 \rangle}$. The highest Pe accessible to us for system size $N = 256$ was determined by examining the scalar gradients in space, and by ensuring that resolution errors in the third and fourth moments of the scalar derivative were at most a few percent. These resolution errors were esti-

TABLE I. Summary of the variances of the scalar gradients and their production term, $\mathbf{g} \cdot \langle \mathbf{v}\theta \rangle$, for OU advection. The total sampling time for which statistics were compiled is denoted by t_r. Errors for moments are estimated as the variance of the time series for the spatially averaged moments divided by $\sqrt{t_r/T}$, assuming approximately one statistically independent sample per turnover time, T.

$Pe \equiv VL/\kappa$ (κ)	N	t_r/T	$\hat{\mathbf{g}} \cdot \langle \mathbf{v}\theta \rangle/(VL)$ $\times 10^{-2}$	$2[\langle (\nabla_\perp \theta)^2 \rangle/(g^2 Pe)]$ $\times 10^{-2}$	$2[\langle (\nabla_\parallel \theta)^2 \rangle/(g^2 Pe)]$ $\times 10^{-2}$
39.3 ± 0.5 (8.064×10^{-2})	128	19.1	5.7 ± 0.5	6.5 ± 0.6	4.9 ± 0.3
97.2 ± 0.2 (3.200×10^{-2})	64	764	6.2 ± 0.1	6.42 ± 0.09	5.92 ± 0.07
246 ± 1 (1.270×10^{-2})	128	191	5.9 ± 0.2	5.9 ± 0.2	6.0 ± 0.1
627 ± 5 (5.040×10^{-3})	256	73.3	6.4 ± 0.4	6.4 ± 0.3	6.4 ± 0.3
1540 ± 20 (2.000×10^{-3})	512	28.6	5.4 ± 0.4	5.3 ± 0.3	5.5 ± 0.3
2700 ± 60 (1.165×10^{-3})	768	4.65	7.2 ± 0.9	6.6 ± 0.8	6.3 ± 0.1

Phys. Fluids, Vol. 6, No. 5, May 1994

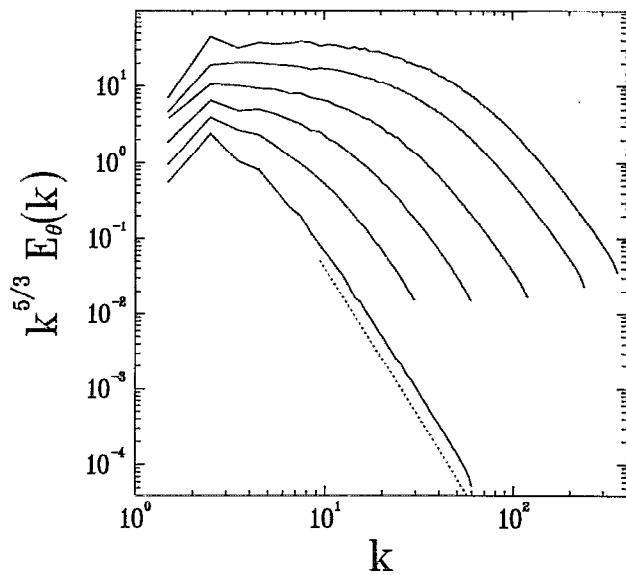M. Holzer and E. D. Siggia   1823

FIG. 1. Normalized spectra of the scalar for OU advection with a $k^{-5/3}$ velocity spectrum for all wave numbers. The spectra have been offset vertically for clarity. The dotted line indicates $k^{-17/3}$. Starting with the lowest curve, the corresponding Péclet numbers and lattice sizes, N, are (Pe, N) = (39.3, 128), (97.2, 64), (246, 128), (627, 256), (1.54×10^3, 512), and (2.70×10^3, 768).

FIG. 2. PDFs of the perpendicular scalar gradients normalized by their RMS value, σ. Since the PDFs must be symmetric, they have been "folded" by plotting $P(\nabla_\perp \theta/\sigma)$ vs $|\nabla_\perp \theta|/\sigma$. The PDFs have been shifted vertically and, starting with the lowest curve, correspond to (Pe, N) = (97.2, 64), (246, 128), (627, 256), (1.54×10^3, 512), and (2.70×10^3, 768). The dashed lines are fits to Eq. (17), with fitting parameters given in Table II. The inset shows a blowup of the center of the PDFs (without folding).

mated by recomputing the moments after setting $\theta_k = 0$ for $|k| > k^*$ and extrapolating the dependence on k^*. The maximum Pe's for systems of other size were determined by scaling the diffusivity such that the ratio of Corrsin scale to grid spacing is constant, i.e., if a system of size N^2 is resolved for diffusivity κ, then a system of size $(N')^2$ is assumed to be equally well resolved for diffusivity $(N/N')^{4/3}\kappa$.

The OU model, when optimized to produce an inertial range as described, gives poor statistics for the scalar itself, which is a large-scale quantity and hence insensitive to the small scales. Under these conditions, we therefore present only scalar spectra and not the scalar PDF.[34] Somewhat unexpectedly, the derivative statistics also converge slowly due to events which are initiated on the large scales and evolve into the ramp-and-cliff features alluded to in Sec. II.[3,4]

Table I shows that our simulations obey the balance between scalar-fluctuation production and scalar dissipation as expressed by Eq. (4), while further demonstrating that the dissipation is isotropic $[\langle (\nabla_\perp \theta)^2 \rangle \simeq \langle (\nabla_\parallel \theta)^2 \rangle]$, and that the source term $g \cdot \langle v\theta \rangle$ has no significant Pe dependence.[35] Thus, $g \cdot \langle v\theta \rangle$ is properly a large-scale quantity, so that by (4) the scalar-gradient variance is proportional to Pe. Figure 1 shows the scalar spectra obtained for
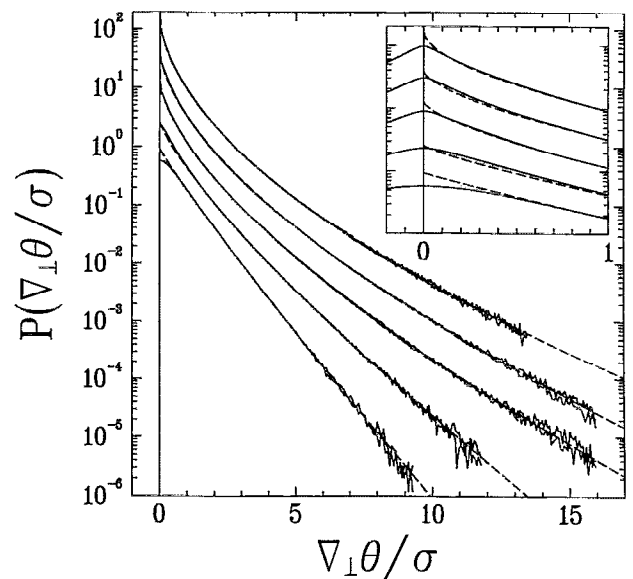
a variety of Pe. We see a $k^{-5/3}$ inertial range over about a decade of wave numbers for the highest Pe, while for the lowest Pe, the predicted velocity-inertial/scalar-diffusive regime of $k^{-17/3}$ is clearly evident. We are thus encouraged to examine the scalar field more closely.

The PDF, $P(\nabla_\perp \theta)$, of the scalar gradient transverse to g is presented in Fig. 2 for several Pe's. Since $\hat{g}$ is the only imposed direction, any asymmetry between $P(\pm |\nabla_\perp \theta|)$ is purely a result of sampling errors. We find that the PDFs can be fit well to the stretched-exponential form,

$$P(\nabla_\perp \theta/\sigma) = \mathcal{N} \exp(-\beta |\nabla_\perp \theta/\sigma|^\alpha), \qquad (17)$$

over a range of $\nabla_\perp \theta$ from a fraction (~ 0.1 for the large Pe) of its root-mean-square (RMS) value, σ, outward. The fits are also shown in Fig. 2, and the corresponding parameters are collected in Table II. The form (17) is at this stage empirical, but has recently also been used for turbulent Rayleigh–Bénard convection to approximate the PDF of temperature differences,[36] and the PDF of the curvature of isothermal and isoconcentration surfaces.[37]

Figure 3 shows the PDF, $P(\nabla_\parallel \theta)$, of the scalar gradient parallel to g. For all Pe shown, $P(\nabla_\parallel \theta)$ is very skewed. The skewness, $S \equiv \langle (\nabla_\parallel \theta)^3 \rangle / \langle (\nabla_\parallel \theta)^2 \rangle^{3/2}$, is tabulated in

TABLE II. Parameters of Eq. (17) for the fits displayed in Fig. 2.

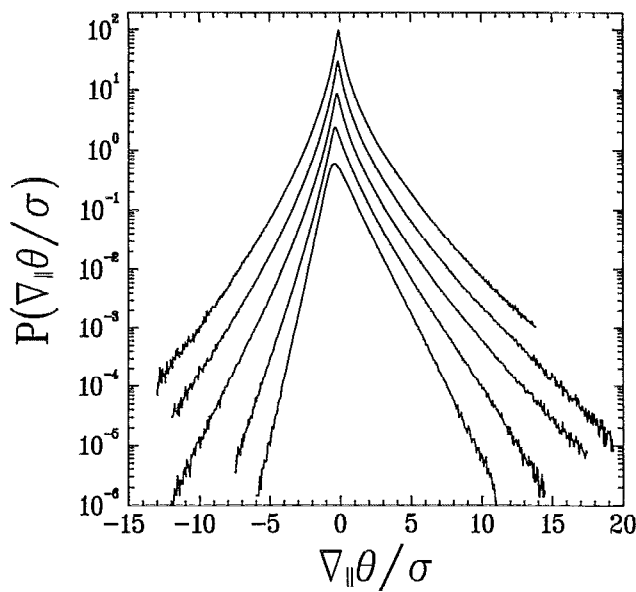| Pe	97.2	246	627	1544	2697
α	0.92 ± 0.01	0.80 ± 0.05	0.661 ± 0.005	0.627 ± 0.005	0.563 ± 0.005
β	1.66 ± 0.05	1.8 ± 0.2	2.39 ± 0.05	2.50 ± 0.05	2.89 ± 0.05

1824   Phys. Fluids, Vol. 6, No. 5, May 1994

M. Holzer and E. D. Siggia

FIG. 3. The parallel-gradient PDFs corresponding to Fig. 2. The Péclet number increases from bottom to top.

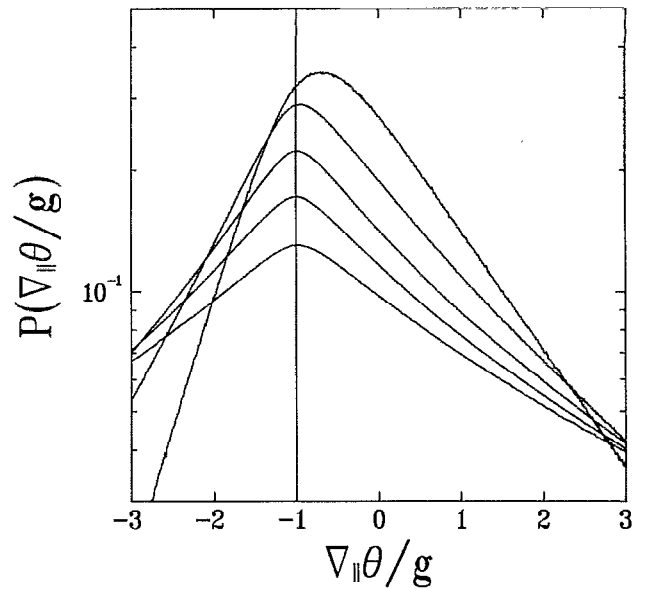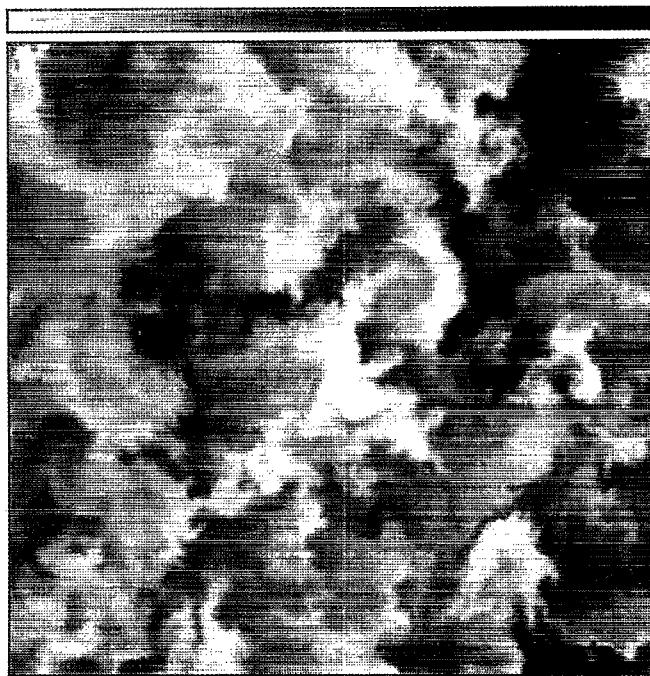FIG. 4. Same as Fig. 3, but with $\nabla_{\|}\,\theta$ plotted in units of the mean gradient, g, and without vertical offset. The Péclet number increases from top to bottom.

Table III. For Pe $\gtrsim 300$, S has very weak Pe dependence and clearly fails to conform to the naive expectation of $S \sim \mathrm{Pe}^{-3/2}$. Also given in Table III are the values of the scalar-gradient kurtosis, $K_{\hat{n}} \equiv \langle (\hat{n} \cdot \nabla\theta)^4 \rangle / \langle (\hat{n} \cdot \nabla\theta)^2 \rangle^2$, for the perpendicular and parallel directions. The kurtoses are $\mathcal{O}(10)$ and increase slowly with Pe.

How does the estimate of $S \sim \mathrm{Pe}^{-3/2}$ fail? The center of $P(\nabla_{\|}\,\theta)$ is shown in Fig. 4, with the gradient plotted on the scale of the external gradient, g. The most probable value of $\nabla_{\|}\,\theta$ [where $P(\nabla_{\|}\,\theta)$ is peaked], rapidly approaches $-g$ with increasing Pe, which means that the velocity field is successful in expelling the mean gradient over most of space. The snapshot of $\theta(\mathbf{x})$ in Fig. 5, and the associated slices through $\theta(\mathbf{x})$ in the direction of the gradient in Fig. 6, clearly show the formation of large-scale ramps in θ with gradient $-\mathbf{g}$. (The slices of Fig. 6 are reminiscent of the temperature time series of Refs. 3, 4, and 26.) The ramps correspond to regions of near-zero total gradient, $\nabla\theta + \mathbf{g}$, and are separated by thin high-gradient cliffs. The cliffs occupy linear, not extensively folded regions in the x-y plane (as defined in Fig. 6).

Typically, a cliff is formed by a convergence of the large-scale flow whose inflow directions have a substantial component along $\hat{\mathbf{g}}$ to establish the overall $\mathcal{O}(gL)$ jump in θ. The cliff is usually well correlated with the separatrices along the outflow from the (instantaneous) stagnation point formed by the convergence (see Fig. 7). (A similar result is shown for the conditionally averaged velocity in Figs. 6 and 7 of Ref. 26.) The scalar appears to be always quite well correlated with the instantaneous streamfunction and, in particular, the fine structure of the cliffs is correlated with the small-scale velocity field. (When the fine structure is suppressed at lower Pe as in Fig. 7, the correlation between the streamfunction and the scalar is actually somewhat more evident to the eye than in Fig. 5.) Inhomogeneities formed by the small-scale velocity are rapidly mixed into the uniform ramp regions which the cliff separates. After a time of order T, the cliffs themselves typically get advected by the large scales into the mixing regions, where they become homogenized while new cliffs are being formed by newly born convergences. Naively, one would think that a sharp feature like the cliffs would thicken with the eddy diffusivity and not with the molecular diffusivity, κ. The cliffs observed, however, are self-generated and definitely conditional on the flow, even though we have no precise analytic way of determining their location. A cliff placed randomly in the flow would broaden in accordance with eddy-diffusivity notions.
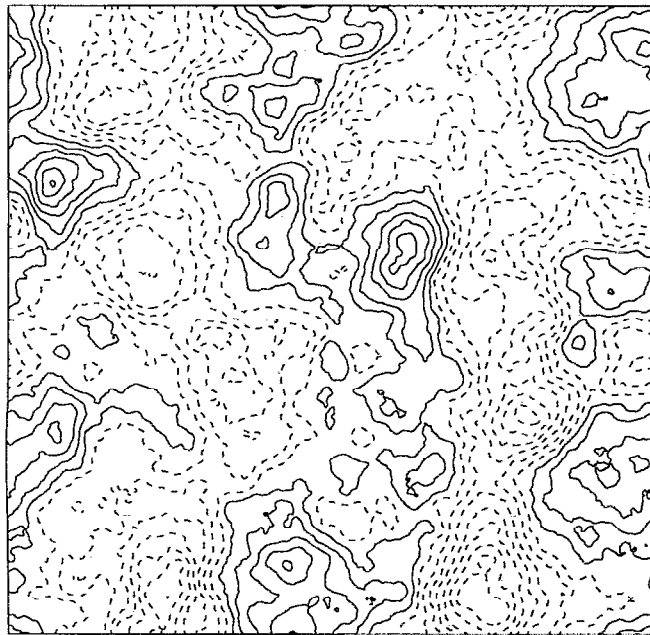
Since our velocity field is not static, there is no obvious reason why the scalar should partition itself with the streamfunction as described other than the fact that the lack of Galilean invariance in our model does in fact single

TABLE III. Skewness and kurtosis of the gradient PDFs for OU advection. Errors were estimated as for Table I.

Pe	39.3	97.2	246	627	1544	2697
S	0.88±0.17	1.31±0.04	1.62±0.11	1.67±0.18	1.51±0.20	1.37±0.46
$K_{\|}$	4.8±1.1	7.03±0.31	10.2±0.91	14.0±2.1	16.1±2.7	17.9±7.7
$K_{\perp}$	3.9±1.2	6.08±0.33	9.01±0.94	12.3±2.1	14.8±2.4	17.6±7.8

Phys. Fluids, Vol. 6, No. 5, May 1994

M. Holzer and E. D. Siggia   1825

min = -2.87107, max = 2.35341

(a)

(b)

FIG. 5. (a) Snapshot of $\theta(\mathbf{x})$ in the stationary state for OU advection at Pe=1544 on a 512^2 lattice. The instantaneous, spatially averaged parallel-gradient skewness of the snapshot is $S=1.01$ (the ensemble-mean skewness is $S=1.51\pm0.20$). The mean gradient is applied in the horizontal and the (linear) gray scale is given in units of gL/π, where L is the integral scale. (b) Evenly spaced contours of the corresponding stream-function.

FIG. 6. Horizontal slices through Fig. 5(a). Note the ramp-and-cliff features which give rise to the net scalar derivative skewness. Plotted in gray is the full scalar, $\Theta=\theta+\mathbf{g}\cdot\mathbf{x}$. Ramps correspond to regions where the mean gradient has been expelled.

out points of convergent flow, where $\mathbf{v}=0$. We defer further discussion on this point until after Sec. V.

To quantify the sharpness of the cliffs, we performed two runs with identical velocity fields but with κ differing by a factor of 2. The cliffs from the two runs then superimpose well, and it is apparent that the height of the cliffs

is insensitive to Pe, while the distribution of the ratio of $\nabla_{\parallel}\,\theta$, at corresponding points within the cliffs, is peaked at $\sqrt{2}$. The scaling of the gradients with $\mathrm{Pe}^{1/2}$ can either be interpreted as a simple consequence of (4) or, more mysteriously, as an instance of Batchelor scaling [cf. Eq. (10)]. While calculation of the RMS strain rate from modes with $2\lesssim k\lesssim4$ does make $\sqrt{\kappa/s}$ a reasonable estimate for the width of the cliffs, we do not yet understand the fundamental reason for their sharpness. The same scaling with $\mathrm{Pe}^{1/2}$ for the width of the spikes in a time trace of the longitudinal scalar derivative was recently noted in experiments on the axis of a jet.[14]

To further elucidate how the skewness arises, we attempted to collapse $f(\nabla_{\parallel}\,\theta)\equiv(\nabla_{\parallel}\,\theta)^3 P(\nabla_{\parallel}\,\theta)$, for the four highest Pe's of Fig. 2, onto a single curve by scaling $\nabla_{\parallel}\,\theta$. No single scale factor suffices, although the position of the positive peaks of $f(\nabla_{\parallel}\,\theta)$ scales reasonably well with $\mathrm{Pe}^{1/2}$. Numerically, the positive peaks occur at 3–4 times the RMS value of $\nabla_{\parallel}\,\theta$.[38] Inspection of numerous snapshots of the scalar shows that the small-scale fluctuations on the ramps definitely increase with Pe but remain symmetric so that they affect the skewness only through its denominator. A conspiracy of factors to which we do not have ready access, except through the skewness, is required to explain the nearly Pe-independent value of S in Table III. We estimate the skewness as

$$S\sim\frac{\Gamma\times(gL/l)^3}{\mathrm{Pe}^{3/2}},\qquad(18)$$

where gL/l is a typical value for the gradient in the cliffs, and Γ is the area fraction of the high-skewness regions. Thus, once we accept that $\nabla_{\parallel}\,\theta\sim l^{-1}\sim\mathrm{Pe}^{1/2}$, the area fraction, Γ, occupied by such points must be Pe independent to give a Pe-independent skewness. Since the number and positioning of the cliffs is controlled by the large scales of motion, the small-scale folding of the cliffs must increase to compensate for their decrease in thickness.

M. Holzer and E. D. Siggia
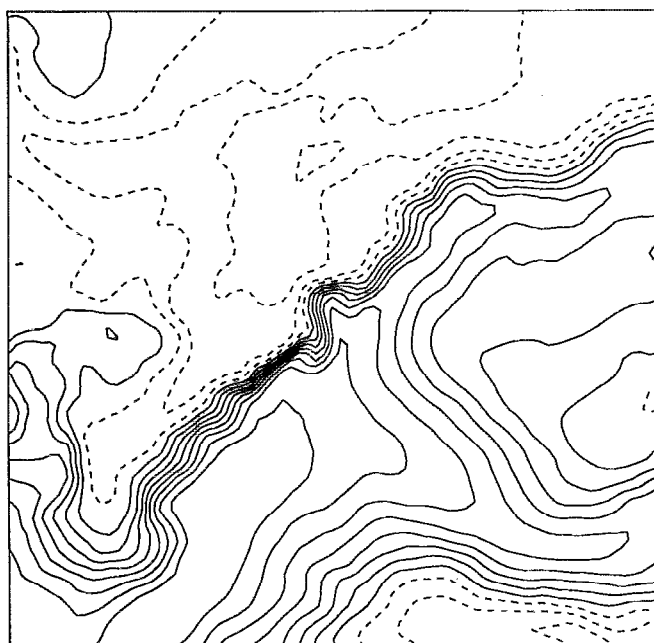
(a)
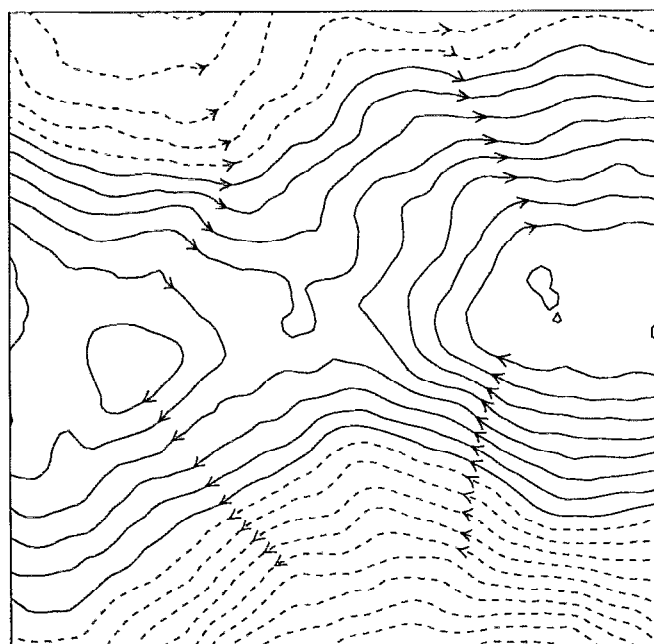
(b)

FIG. 7. (a) Contours of $\theta(x)$ spaced by $0.4(gL/\pi)$ for OU advection on a 256^2 lattice with $\kappa = 5.040 \times 10^{-3}$ (Pe$=627 \pm 5$). The region shown is 78 mesh spacings (or $\sim 0.61L$) on a side and contains a well-developed cliff. (b) Evenly spaced contours of the corresponding streamfunction.

Because the high gradients are concentrated on the boundary of roughly compact integral volumes, $(\nabla_\parallel \theta)^3$ averaged spatially, should change on the integral time. As Fig. 8 shows, this is in fact what is observed not only for the third moment, but also for the dissipation and the fourth moment. Thus, we essentially get only one independent sample per integral time, which explains the large error bars in Tables I and III.[35]

It is encouraging that our S(Pe) behaves roughly as in real experiments.[3–5,11] We believe that this is not due to the
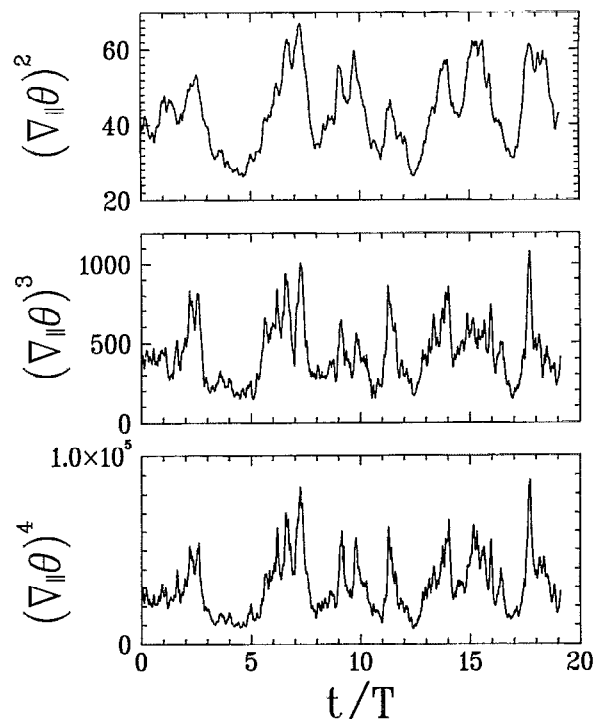
FIG. 8. Time series of $(\nabla_\parallel \theta)^2$, $(\nabla_\parallel \theta)^3$, and $(\nabla_\parallel \theta)^4$ spatially averaged for OU advection at Pe$=1.54 \times 10^3$. The moments of the instantaneous parallel-gradient PDF have large fluctuations on the scale of the integral time, T, and are clearly correlated (especially the third and fourth moments).

pathologies of the OU model. In order to reduce the inherent sweeping effect, we have rerun the case of $\kappa = 5.040 \times 10^{-3}$ and $N = 256$ with $\gamma(k) \rightarrow 4\gamma(k)$, keeping V fixed at what is was before. This enhances the estimated eddy diffusivity, $\kappa_e(r)$, [Eq. (14)] by a factor of 4 for all r by decreasing the autocorrelation time of the velocity and hence the sweeping. We find that the character of the spatial structure of the scalar remains unchanged and that the skewness remains $\mathcal{O}(1)$ although it is reduced by $\sim 40\%$ to $S = 1.13 \pm 0.15$.

V. RESULTS FOR RESTRICTED EULER ADVECTION

For the scalar itself, we need many integral scales to improve statistics and to mitigate artifacts of the periodic boundary conditions, while having enough resolution for adequate dissipation. We were able to balance these conflicting requirements for model (16) on a 128^2 lattice by choosing $(k_{min}, k_{max}) = (4, 8)$, and by using a hyperdissipation, $\widetilde{\kappa} k^4 \theta(k)$, instead of $\kappa k^2 \theta(k)$. The k^4 diffusion should have no effect on the large-scale physics. The resulting stationary distribution is shown in Fig. 9. Exponential tails are clearly evident and the kurtosis of $K = 3.6 \pm 0.3$ and general shape of the PDF are consistent with what is seen experimentally.[9,10] The transient PDFs, computed by repeatedly letting the scalar relax from $\theta(x) = 0$ for a fixed time $t \lesssim 3T$, have more pronounced tails than in Fig. 9, with kurtoses $K \sim 4.0$–4.2.
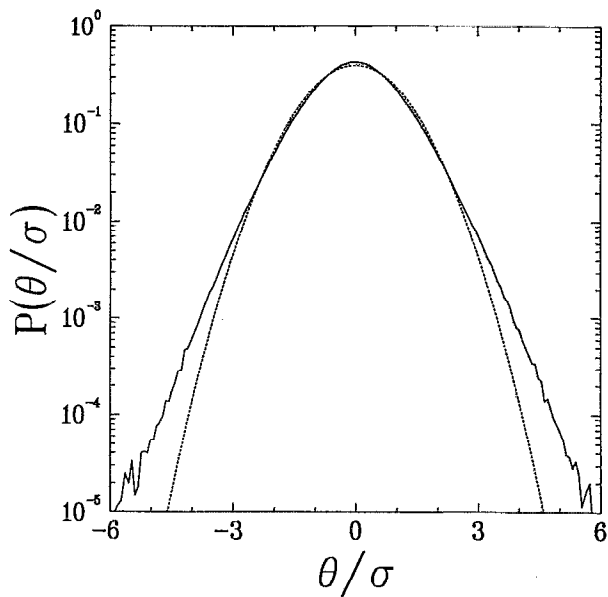
FIG. 9. The PDF of the scalar for restricted Euler advection with $(k_{min}, k_{max}) = (4, 8)$ on a 128^2 lattice. The scalar was dissipated by a $\tilde{\kappa} k^4 \theta_k$ hyperdiffusion with $\tilde{\kappa} = 1.5 \times 10^{-6}$. The PDF shown has RMS value $\sigma/(gL) = 0.74 \pm 0.01$, kurtosis $K = 3.6 \pm 0.3$, and was computed from $\theta(x)$ after modes with $k < 4$ were discarded. The dotted line indicates a Gaussian of the same variance. The filtering does not change the qualitative shape of the PDF; for unfiltered data it has $\sigma/(gL) = 0.83 \pm 0.01$ and $K = 3.4 \pm 0.3$.
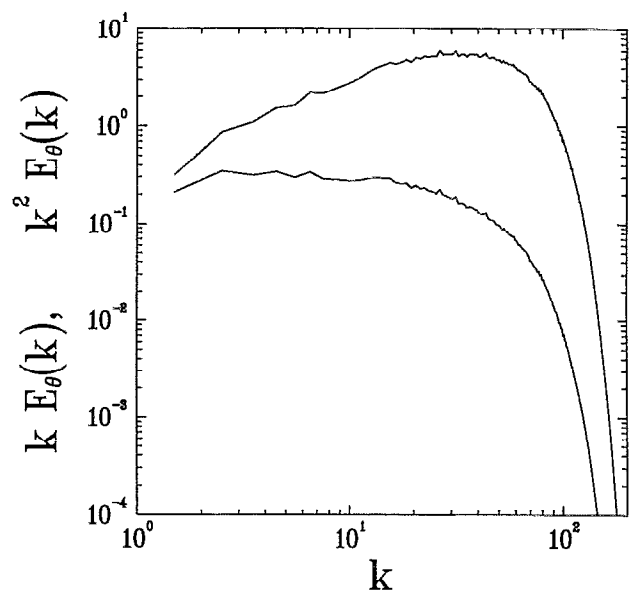
FIG. 10. The normalized dissipation spectrum (top curve) and scalar spectrum in the Batchelor regime. The scalar was advected by the restricted Euler model with $(k_{min}, k_{max}) = (1, 3)$ on a 512^2 lattice and dissipated by a $\tilde{\kappa} k^4 \theta_k$ hyperdiffusion with $\tilde{\kappa} = 3.0 \times 10^{-8}$.

Since the k^{-1} spectrum predicted by Batchelor[20] has proved elusive experimentally, we search for it numerically by moving the wave-number band (k_{min}, k_{max}) back to (1, 3), which gives us ten independent velocity modes.[39] Since no argument for the k^{-1} regime makes any demands on the form of the dissipation, provided it is strong enough, we again utilize a k^4 hyperdiffusivity to maximize the scale range. Figure 10 shows that, on a 512^2 lattice with $\tilde{\kappa} = 3 \times 10^{-8}$, we can push the peak of the dissipation spectrum out to $k \sim 30$. The beginning of a k^{-1} regime over about a decade of wave numbers is clearly evident for the scalar spectrum. Figure 11 shows a snapshot of the scalar and the corresponding streamfunction under the same conditions. The scalar has the same layered, streaky character as is observed in experiments on scalar mixing in axisymmetric jet turbulence at high Schmidt number.[7] Unfortunately, the scalar spectra are not available for those experiments. Except for the integral-scale jelly-roll-like structures, the scalar is in detail *not* well correlated with the instantaneous streamlines. We find that the scalar gradients still have a skewness of 0.44 ± 0.22, which is less apparent than in Fig. 5(a) since $\langle (\nabla_\parallel \theta)^2 \rangle / g^2 = (1.7 \pm 0.2) \times 10^3$, versus 42 ± 2 in Fig. 5(a). Because the k^4 diffusivity does not allow us to attach much physical meaning to the gradient PDFs, especially for large gradients, we merely note that they are rounded for gradients of order g although they appear cusped on the scale of their RMS value.

It is interesting to study the derivative PDFs for what is effectively the large Pr limit. To obtain realistic values of

the gradient for large fluctuations, we return to the physical Laplacian diffusion and also move the velocity band in (16) out to $(k_{min}, k_{max}) = (4, 6)$ to improve statistics $(k_0 = 5)$. We define a physical $Pe = VL/\kappa$ with the RMS velocity V and $L \equiv 2\pi/k_0$. The scalar gradients are resolved with $Pe \sim 320$ on a 256^2 lattice or, via Eq. (10), $Pe \sim 1280$ on a 512^2 lattice. Figure 12 shows the scalar spectra obtained for $Pe = 62.8$, 314, and 1257 on a 128^2, 256^2, and 512^2 lattice, respectively. Although there is a trend with increasing Pe toward a k^{-1} spectrum, we no longer have a sufficiently large range of scales to observe Batchelor scaling.

The perpendicular-gradient PDFs corresponding to the spectra of Fig. 12, together with fits to Eq. (17), are shown in Fig. 13. In the concave region of $P(\nabla_\perp \theta)$, the fits are reasonable down to gradients as small as $\sim 0.1\sigma$. For gradients larger than about 5–6σ, the stretched-exponential region crosses over to another functional form which is plausibly exponential. We expect the crossover point to be determined by $g^* \equiv \tilde{\theta} \sqrt{s/\kappa}$, since the scalar cannot be compressed by the strain s to distances less than $\sqrt{\kappa/s}$. Using for s the RMS value for the strain in our model, and for $\tilde{\theta}$ the RMS value of θ (which is roughly Pe independent), we indeed obtain a value of $g^* \sim 6\sigma$ (e.g., for Pe $= 1257$, we have $\sigma \sim 8.5$, $s \sim 2.6$ and $\langle \theta^2 \rangle \sim 1.0$, in units where $g = 1$).

The parallel-gradient PDFs, corresponding to Fig. 13 are shown in Fig. 14. In Fig. 15, we have replotted their centers with $\nabla_\parallel \theta$ in units of g. Even on the scale of g, the PDFs have a very sharply peaked center, with the intermediate Pe curve being the sharpest. It is illuminating to look at corresponding snapshots of the scalar, which are shown in Figs. 16–18. Although more structure appears with increasing Pe, there is remarkably little structure

M. Holzer and E. D. Siggia

min = -16.4419, max = 12.4588
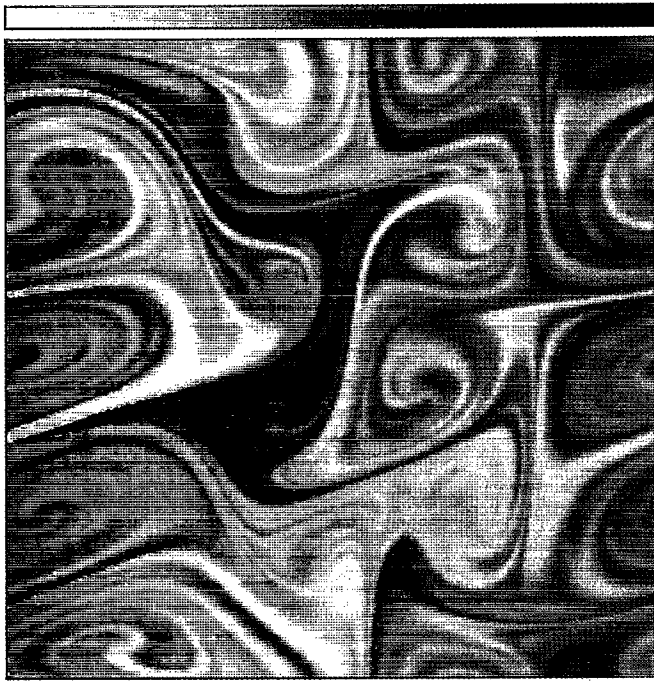
(a)
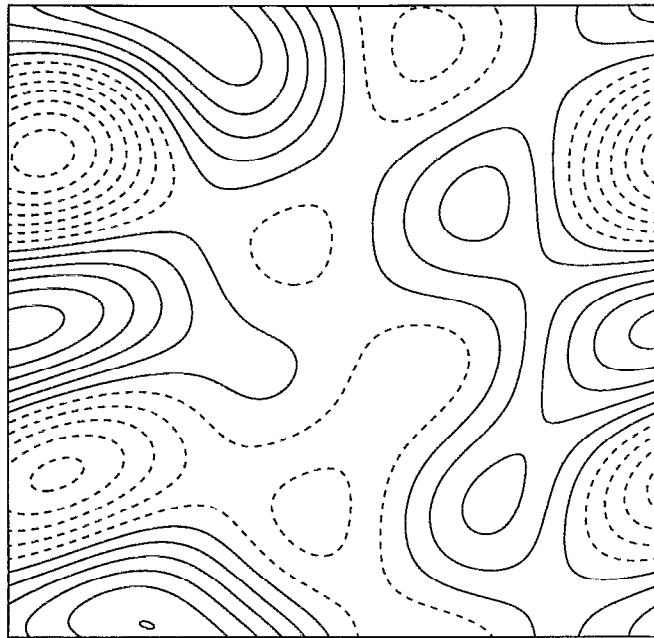
(b)

FIG. 11. (a) Snapshot of $\theta(x)$ in the Batchelor regime under the same conditions as for Fig. 10. The mean gradient is applied in the horizontal and the gray scale is given in units of gL/π. (b) Evenly spaced contours of the corresponding streamfunction.
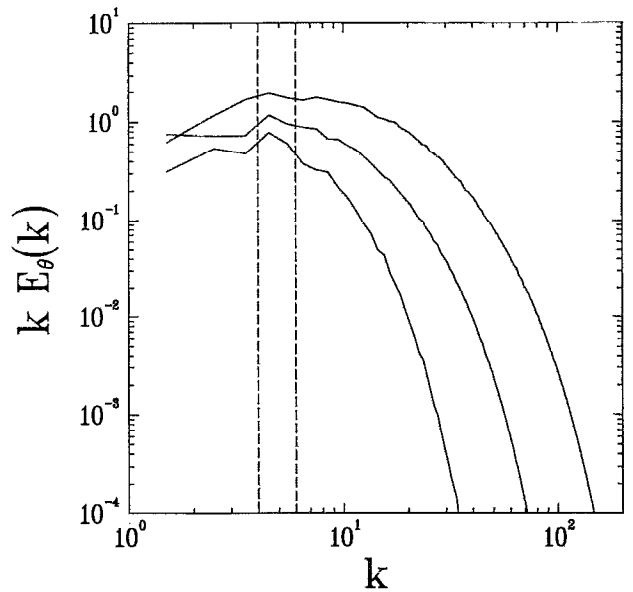

FIG. 12. Normalized spectra of the scalar for restricted Euler advection with $(k_{\min}, k_{\max}) = (4, 6)$ as indicated by the dashed lines. The spectra have been offset vertically for clarity. Starting with the lowest curve, the corresponding Péclet numbers and lattice sizes, N, are $(Pe, N) = (62.8, 128)$, $(314, 256)$, and $(1257, 512)$.

We have the following physical picture for these observations. Since our velocity field is time dependent and has generally both strain and shear, we expect eddies to mix the scalar in a time $\sim T \log(Pe)$ (as opposed to the
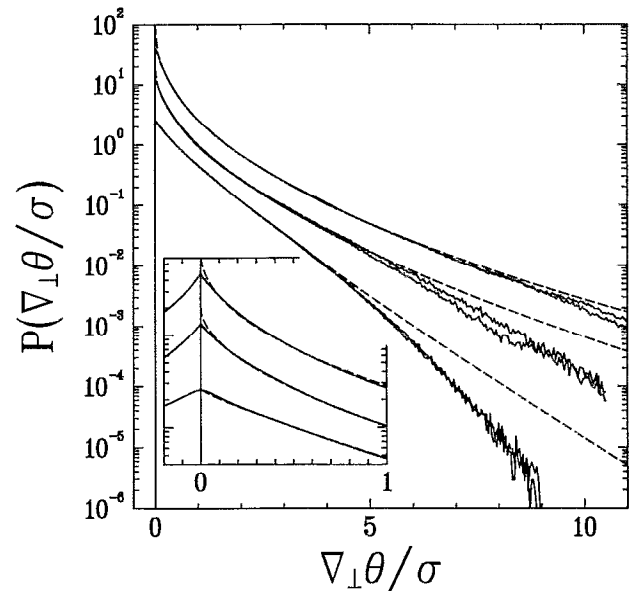

FIG. 13. PDFs of the perpendicular gradients for restricted Euler advection with $(k_{\min}, k_{\max}) = (4, 6)$, natural time scale, and physical dissipation. The curves have been "folded" as in Fig. 2 and are offset vertically. Starting with the lowest curve, they correspond to $Pe = 62.8$, 314, and 1257. The dashed lines are fits to Eq. (17) with parameters $(\alpha, \beta) = (0.85 \pm 0.02, 1.7 \pm 0.1)$, $(0.55 \pm 0.02, 2.9 \pm 0.1)$, and $(0.46 \pm 0.01, 3.6 \pm 0.2)$ in order of increasing Pe. The inset shows a blowup of the center of the PDFs (without folding).
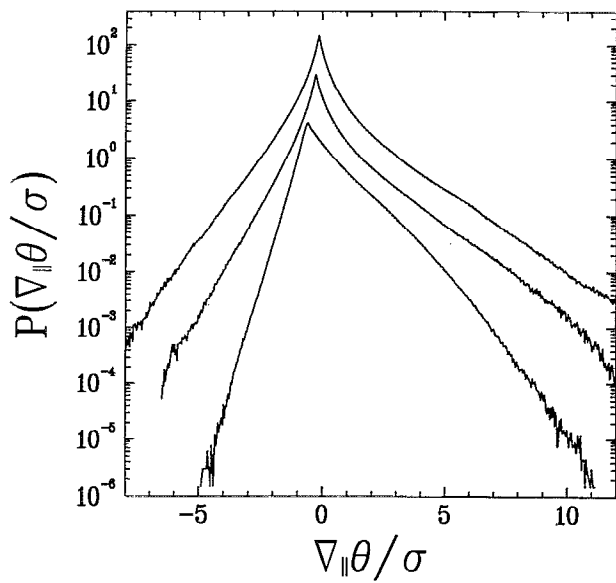
across an eddy even at the highest Pe, and the gradients occur mostly in the high-strain regions around (instantaneous) stagnation points (see, e.g., the top of Fig. 18). Thus, for the Pe studied, the velocity evolving on its natural time scale is very successful at expelling the mean scalar gradient and concentrating it in cliffs. The sharpness of the gradient PDFs is attributable to the large areas with little variation in θ.

FIG. 14. PDFs of the parallel gradients corresponding to Fig. 13. The Péclet number increases from bottom to top.

much slower time $\sim T \, \mathrm{Pe}^{1/3}$ for pure shear[40]). Thus, for small Pe, the scalar has time to get completely homogenized in the interior of an eddy during an integral time, T, whereas for large Pe, there is no longer sufficient time to mix the scalar entirely during an autocorrelation time of the velocity so that differential rotation begins to produce a jelly-roll-like structure (Fig. 18). The fact that the gradient PDF is sharpest for Pe$\sim$300 suggests that, for this value of Pe, integral and mixing times are particularly well matched. Nevertheless, for all Pe studied the high correlation of the scalar with instantaneous streamlines indicates
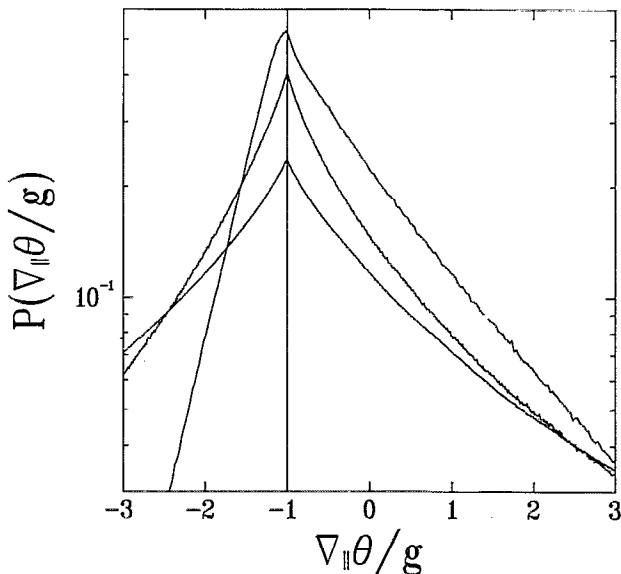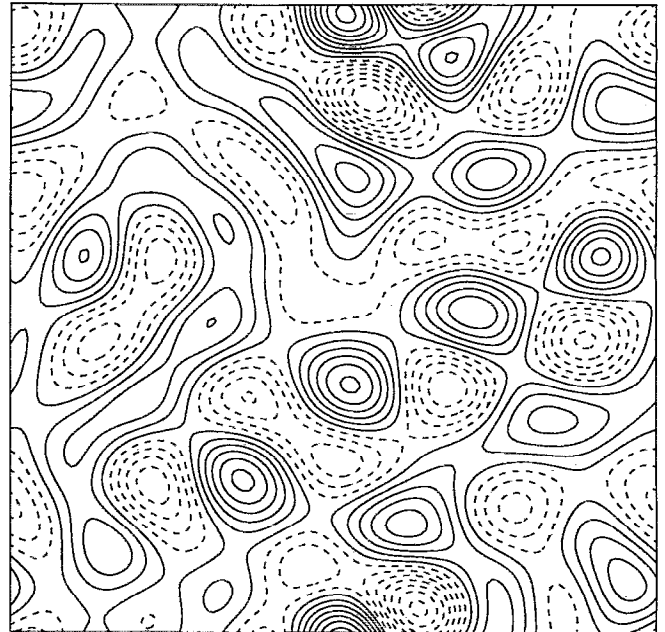

FIG. 15. Same as Fig. 14 but with $\nabla_\parallel \theta$ plotted on the scale of the mean gradient, g, and without vertical offsets. The Péclet number increases from top to bottom.

min = −1.30313, max = 1.62033

(a)

(b)

FIG. 16. (a) Snapshot of $\theta(\mathbf{x})$ in the stationary state at Pe=62.8 on a 128^2 lattice. The scalar is advected by the restricted Euler model on its natural time scale with $(k_{\min}, k_{\max}) = (4, 6)$. The mean gradient is applied in the horizontal and the gray scale is given in units of $5gL/(2\pi)$. (b) Evenly spaced contours of the corresponding streamfunction.
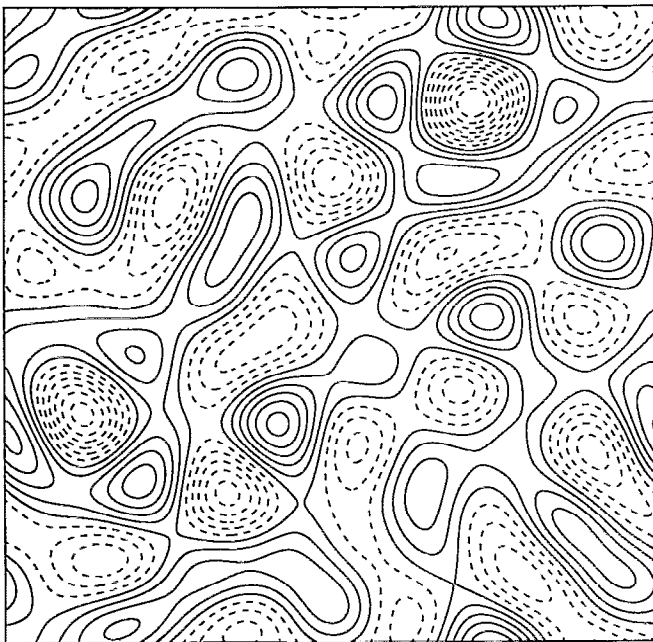
that the mixing time was $\mathscr{O}(T)$. For very high Pe, which was in effect achieved in Fig. 11 through the use of k^4 diffusion, random straining and differential rotation dominate giving rise to the k^{-1} Batchelor regime.

Figure 19(a) shows the PDF of the dissipation, $P(z \equiv |\nabla \theta|^2/\sigma)$, for Pe=1257. Since the PDF of the gradients is not lognormal, we do not expect $P(z)$ to be log-

(a)

(b)

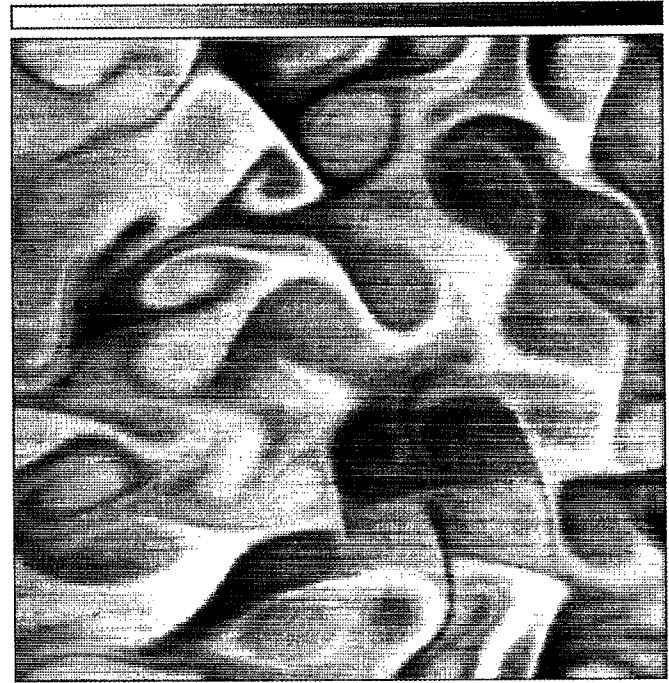FIG. 17. (a) and (b) As for Fig. 16, but with Pe=314 on a 256^2 lattice.

(a)

(b)

FIG. 18. (a) and (b) As for Fig. 16, but with Pe=1257 on a 512^2 lattice.

normal. In fact, if both $\nabla_{\perp}\theta$ and $\nabla_{\parallel}\theta$ were purely stretched exponential with the same β and exponent α [Eq. (17)], one obtains for their convolution (assuming the two components of the gradient are statistically independent),
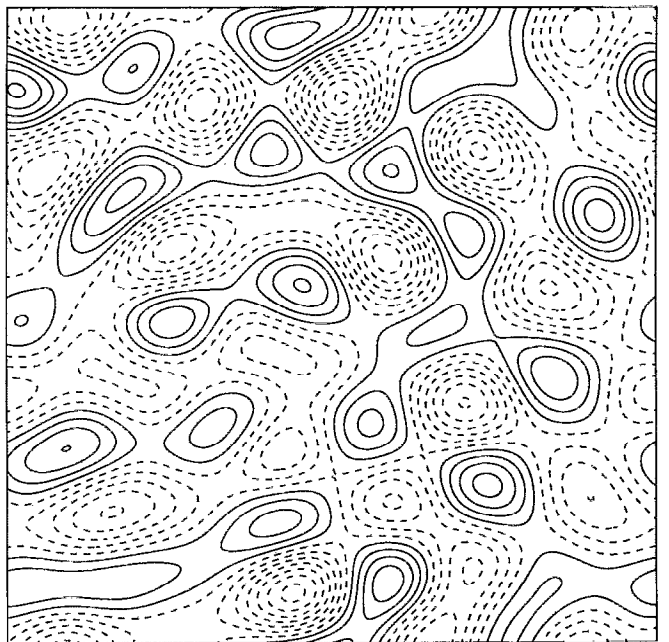
$$P\left(z=\frac{|\nabla\theta|^2}{\sigma}\right)=4\sigma\mathcal{N}^2\int_0^{\pi/4}d\xi$$

$$\times\exp[-\beta z^{\alpha/2}(\cos^\alpha\xi+\sin^\alpha\xi)].$$

For small z this reduces to $P(z)\sim\pi\sigma\mathcal{N}^2[1-(\text{const})z^{\alpha/2}]$, while for large z, $P(z)\sim\mathcal{N}z^{-1/2}\exp(-\beta z^{\alpha/2})$. The latter

expression fits the data over about 1–15σ. It is worth noting that the small-z dependence of $P(z)$ depends on dimensionality. In D dimensions, $P(z)\to z^{(2-D)/2}$ as $z\to0$, again assuming D statistically independent components of $\nabla\theta$. Thus, in 3D, $P(z)$ diverges like $z^{-1/2}$ as $z\to0$ (Ref. 14), unlike in 2D, where $P(z=0)$ is finite and nonzero.

As a test of lognormality, we show in Fig. 19(b) $P[\log(z)]=zP(z)$ vs z on a log–log plot, as is conventional.[14] The discreteness of our bins prevents us from seeing $P[\log(z)]\to z$ as $\log(z)\to-\infty$, but the PDF is not expected to be lognormal in this limit for the reasons
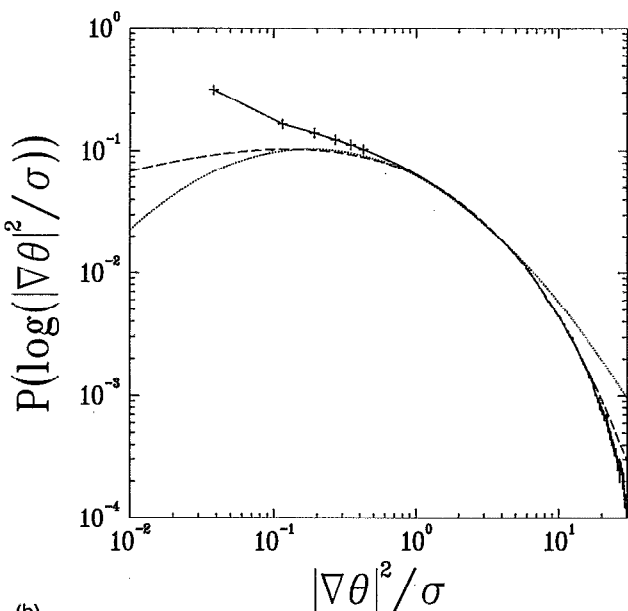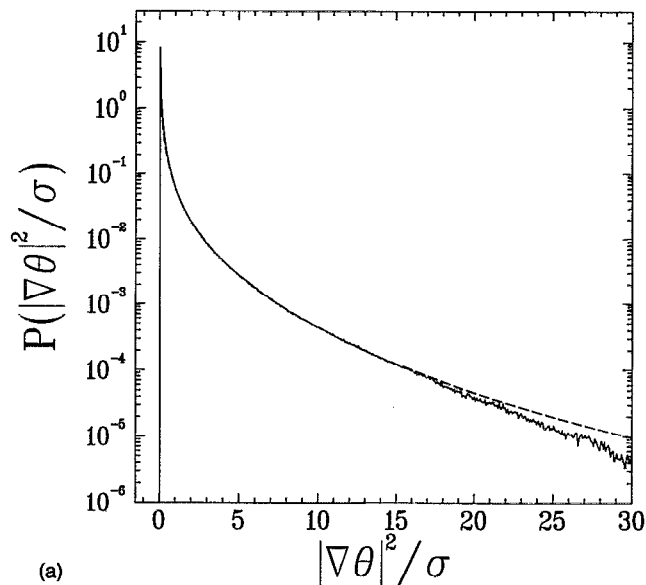
(a)

(b)

FIG. 19. (a) PDF of the dissipation, $|\nabla\theta|^2$, normalized by its variance, σ, corresponding to the conditions of Fig. 18 (solid line). The dashed line is a fit to (const) $|\nabla\theta|^{-1}\exp[-\beta(|\nabla\theta|^2/\sigma)^{\alpha/2}$ with $(\alpha/2, \beta) = (0.36 \pm 0.02, 2.93\pm0.25)$ as derived in the text for large dissipation. (b) A log–log plot of the PDF of the logarithm of the dissipation showing a "fit" to a parabola as a test of lognormality (dotted line). For small dissipation, the location of the histogram bins is shown by crosses, and the other curves are as in (a).

noted above. For large z, the lognormal form falls less rapidly than a stretched exponential and therefore is a poorer fit.

The white-noise limit of the velocity in the Batchelor regime is interesting because it facilitates theory[13,23] and allows one to quantify how the cusps in Fig. 15, and the sharp fronts in Figs. 16–18, depend on the persistence of the eddies. White noise is also the furthest removed from a frozen velocity, which in 2D has the undesirable property of closed Lagrangian trajectories. Thus, simulations in the
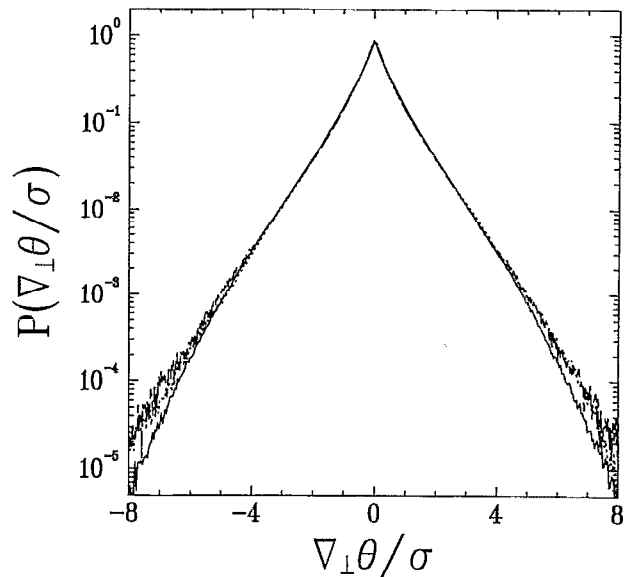

FIG. 20. Approach to the white-noise limit $(\eta \to \infty)$ at $Pe_\tau = 62.8$ of $P(\nabla_\perp \theta)$ for restricted Euler advection with $(k_{min}, k_{max}) = (4, 6)$. The solid curve corresponds to $\eta = 1$, the dashed curve to $\eta = 5$, and the dotted curve to $\eta = 20$.

white-noise limit provide some indication of the possible systematic errors inherent in our model. We adjust the autocorrelation time of the velocity, τ, by multiplying the advective term in (16) [but not in (2)!] by a speed-up factor $\eta \propto \tau^{-1}$. The white-noise limit, $\eta \to \infty$, should be taken at fixed Taylor diffusivity,[30] $D \sim V^2\tau \sim VL/\eta$, or, equivalently, at fixed $Pe_\tau \equiv VL/(\eta\kappa)$. With this definition, $\langle|\nabla\theta|^2\rangle$ has a sensible limit, $(1/2)Dg^2/\kappa$, which follows from (4) since $\langle v_\parallel \theta\rangle$ can be evaluated exactly for $\tau \to 0$ by using

$$\theta[x_\alpha(t),t] = \theta[x_\alpha(t-\Delta t),t-\Delta t]$$
$$+ \hat{g} \cdot \int_{t-\Delta t}^{t} v[x_\alpha(t'),t']dt' + \mathscr{O}[(\Delta t)^2],$$

(19)

where x_α is a Lagrangian point.

We approached the white-noise limit with a series of runs for $\eta = 1, 5$, and 20, with V fixed and $\kappa \propto \eta^{-1}$, so that Pe_τ was constant and equal to 62.8. The PDFs of $\nabla_\perp \theta$ in Fig. 20, and $\nabla_\parallel \theta$ in Fig. 21, normalized with their respective RMS value, σ, seem to converge to a limiting form. The convergence of σ is surprisingly slow, e.g., for $P(\nabla_\perp \theta)$ we obtain $\sigma/g = 1.661 \pm 0.008$, 3.65 ± 0.10, and 6.78 ± 0.12 in order of increasing η. Figure 22 shows the center of $P(\nabla_\parallel \theta)$ on the scale of g. While the most probable value of the parallel gradient is $-g$ in all cases, the centers round with decreasing τ. This is also apparent in the snapshot of $\theta(x)$ of Fig. 23, which shows that the scalar for $\eta = 20$ has more structure than for $\eta = 1$ and no correlation with the instantaneous velocity field. Despite the banded texture of
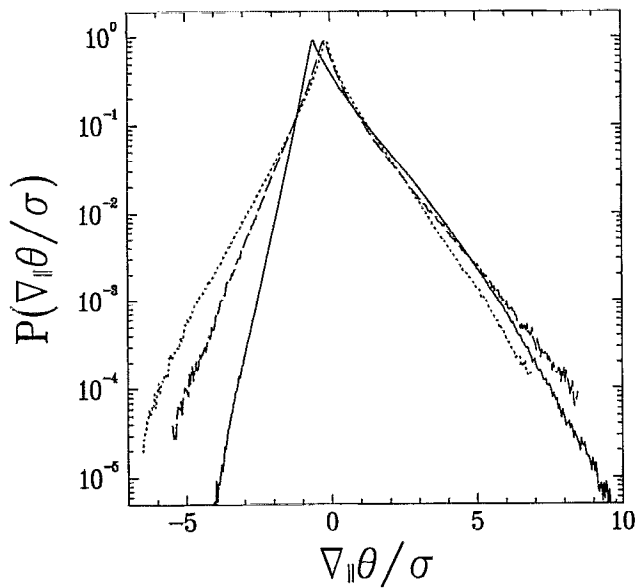
M. Holzer and E. D. Siggia

FIG. 21. Same as Fig. 20 for the parallel gradients, $\nabla_\parallel \theta$.

the scalar in Fig. 23, its spectrum is virtually identical to that obtained for the same parameters but $\eta = 1$ (cf. Fig. 12).

Finally, to get an idea of the systematic dependence of the gradient PDF on Pe_τ in the white-noise limit, we show superposed in Fig. 24 three transverse gradient PDFs on the scale of g for $\eta = 20$ and $\mathrm{Pe}_\tau = 3.14$, 15.7, and 62.8. While for small Pe_τ the most probable value of the parallel gradient is significantly larger than $-g$, the rounding of the centers of the PDFs is roughly Pe independent.

Table IV summarizes the variance, skewness, and kurtosis data for the numerical experiments of this section
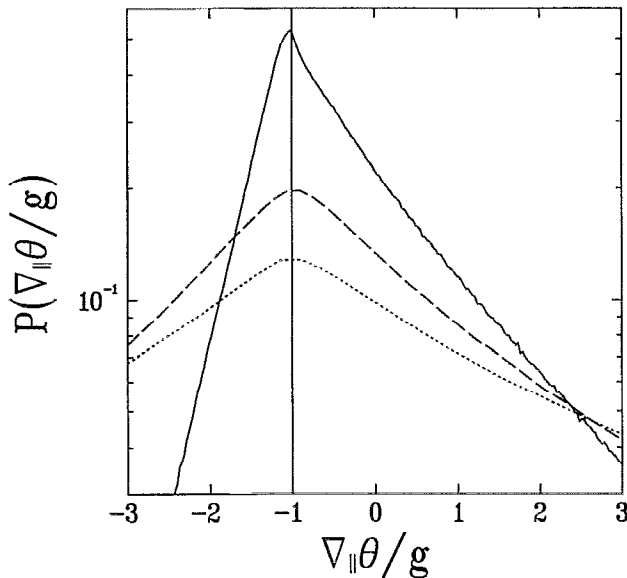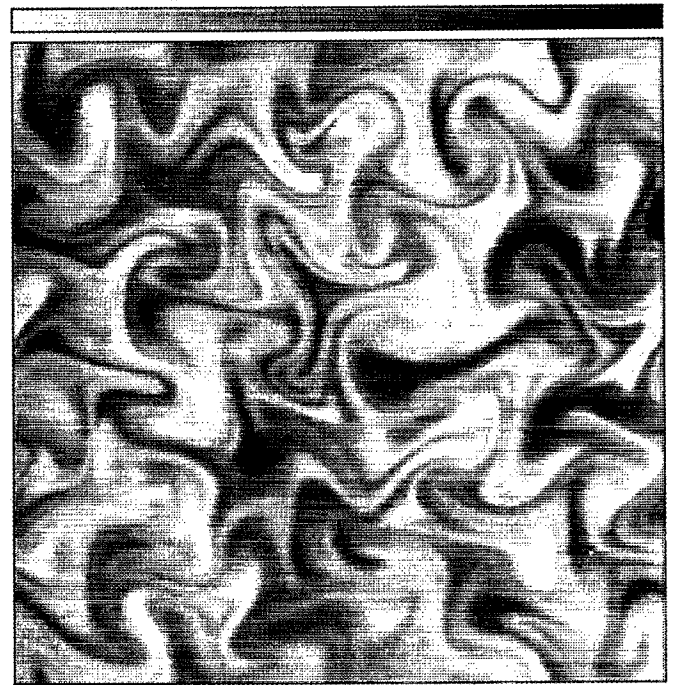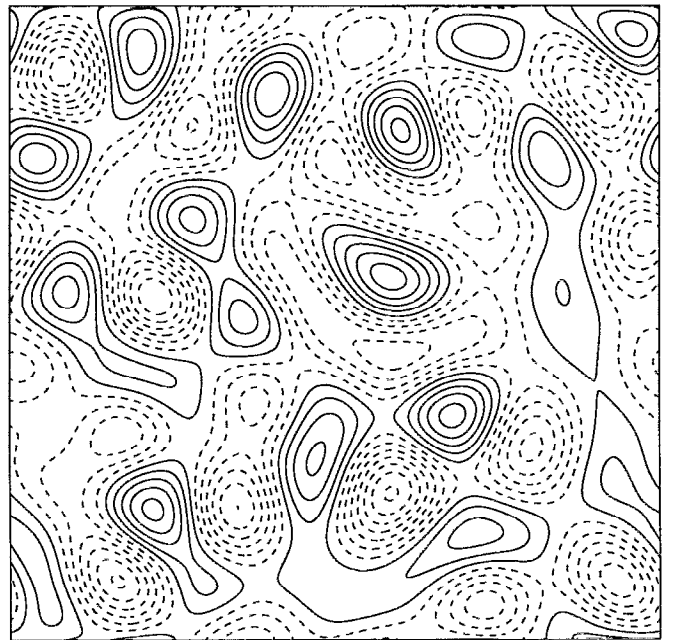

FIG. 22. Same as Fig. 21 but with $\nabla_\parallel \theta$ plotted on the scale of the mean gradient, g.

(a)

(b)

FIG. 23. (a) Snapshot of $\theta(\mathbf{x})$ in the stationary state at $\mathrm{Pe}_\tau = 62.8$ on a 512^2 lattice when advected with the restricted Euler model $[(k_{\min}, k_{\max}) = (4, 6)]$ sped up by a factor of $\eta = 20$. The mean gradient is applied in the horizontal and the gray scale is given in units of $5gL/(2\pi)$. (b) Evenly spaced contours of the corresponding streamfunction.

which were run with Laplacian dissipation and $(k_{\min}, k_{\max}) = (4, 6)$. For advection on the natural time scale, the skewness is virtually Pe independent. When the autocorrelation time of the velocity is decreased by a factor of 20, the skewness decreases by a factor of ~ 2–4.

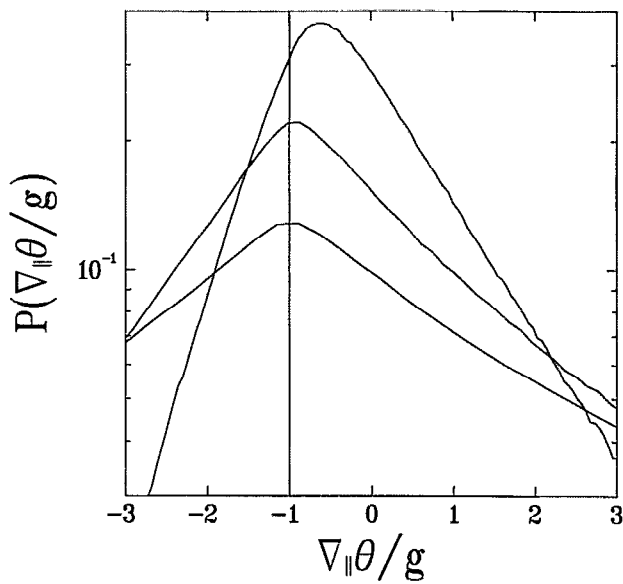For the Pe studied, we infer that the mixing time is sufficiently fast compared with T due to numerical factors,

FIG. 24. Centers of $P(\nabla_{\parallel} \theta)$ for restricted Euler advection [$(k_{min}, k_{max}) = (4, 6)$] which was sped up by a factor of $\eta = 20$. Starting with the top curve, the Péclet numbers and lattice sizes, N, are $(\text{Pe}_\tau, N) = (3.14, 128)$, $(15.7, 256)$, and $(62.8, 512)$.

skewness production also suggests that the skewness will decrease with the velocity correlation time as observed.

In the limit $\text{Pe} \to \infty$, with the time scale for the velocity fixed, we expect the skewness to go to zero as $\text{Pe}^{-1/2}$. This follows if the cliffs remain smooth as they thin, so that the area fraction, Γ, occupied by the cliffs decreases as $\text{Pe}^{-1/2}$. Because the characteristic value of $\nabla_{\parallel} \theta$ which enters both the numerator and denominator of the skewness scales as $\text{Pe}^{1/2}$, the Pe dependence of $(gL/l)^3$ in Eq. (18) cancels. The nearly Pe-independent skewness displayed in Table IV is likely due to a lengthening of the cliffs. [The dissipation, while not occurring uniformly in space, scales as Pe^1 (Table IV).] Barring subtle effects not apparent for the Pe studied, we believe, however, that the length of the high-skewness regions stabilizes at asymptotically high Pe to give $S \sim \text{Pe}^{-1/2}$ when the k^{-1} spectrum is fully developed.

VI. SUMMARY AND CONCLUSIONS

The scalar spectra found numerically are consistent with the standard theoretical predictions in spite of the artificiality of our velocity fields. With the highest range of scales attainable in our simulations, we can identify for effectively small Pr a $k^{-5/3}$ scalar-inertial range followed by a velocity-inertial/scalar-diffusive $k^{-17/3}$ cascade, while for effectively large Pr, we find Batchelor's k^{-1} spectrum. The scaling regions extend over about a decade in wave number.

It is surprising how well the shape of our gradient PDFs compare with laboratory experiments in much more complicated settings.[36,42] For instance in Fig. 25, we show a fit of the stretched-exponential form (17) to the time derivative of the temperature in the center of a helium convection cell at high Rayleigh number.[36,42] The data is very similar for an off-center probe,[36] where there is a mean flow[42] which allows the time derivative to be interpreted as a spatial one. Note the striking similarity with Fig. 2 as well as the resemblance to Fig. 13 for $|\nabla_{\perp} \theta| \lesssim 5\sigma$.

The scalar-gradient PDF has several regimes marked

so that the scalar is homogenized within eddies and the gradient expelled to the vicinity of the open streamlines. The correlation between the scalar and the instantaneous streamfunction is reminiscent of what occurs for a static array of rolls,[41] although the time dependence in our problem ultimately means that the mixing time should scale as $T \log(\text{Pe})$ rather than $T \text{Pe}^{1/3}$. In our simulations, the cliffs appear to follow the time-dependent separatrices which emerge from the saddle points. Selected fluid parcels, initially spaced by $\mathcal{O}(L)$ along $\hat{g}$, which converge in the hyperbolic regions, where the strain, s_L, is high, spend sufficient time there so that the gradient can grow exponentially [like $\sim \exp(2s_L t)$] to the maximum value, $\sim \sqrt{\kappa/s_L}$, allowed by the diffusivity. This picture for the

TABLE IV. Summary of the variances, skewnesses, and kurtoses of $P(\nabla_{\perp} \theta)$ and $P(\nabla_{\parallel} \theta)$ for Euler advection with the velocity restricted to the band $(k_{min}, k_{max}) = (4, 6)$, $L \equiv 2\pi/5$. Errors were estimated as for Table I.

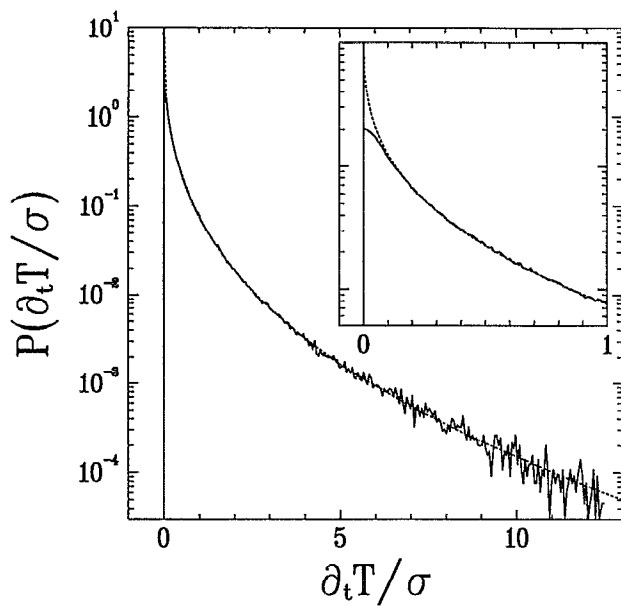| $\text{Pe}_\tau \equiv VL/(\kappa\eta)$ (κ)	η	N	t_r/T	$\langle(\nabla_{\perp}\theta)^2\rangle g^{-2}$	$\langle(\nabla_{\parallel}\theta)^2\rangle g^{-2}$	S	$K_{\perp}$	$K_{\parallel}$
62.8 (2.0×10^{-2})	1	128	955	2.76 ± 0.03	3.12 ± 0.02	1.80 ± 0.04	6.7 ± 0.3	7.9 ± 0.2
314 (4.0×10^{-3})	1	256	95.5	13.2 ± 0.4	15.0 ± 0.4	2.4 ± 0.2	12 ± 2	15 ± 2
1257 (1.0×10^{-3})	1	512	24.6	51 ± 2	53 ± 2	2.3 ± 0.3	19 ± 4	20 ± 3
62.8 (4.0×10^{-3})	5	256	23.9	13.3 ± 0.7	15.4 ± 0.7	2.5 ± 0.4	14 ± 3	16 ± 3
3.14 (2.0×10^{-2})	20	128	31.8	2.27 ± 0.06	2.51 ± 0.08	1.1 ± 0.1	4.3 ± 0.5	5.9 ± 0.8
15.7 (4.0×10^{-3})	20	256	7.96	11.6 ± 0.6	12.8 ± 0.6	1.1 ± 0.2	7 ± 1	8 ± 2
62.8 (1.0×10^{-3})	20	512	3.18	46 ± 2	48 ± 3	0.6 ± 0.2	7 ± 1	7 ± 2

M. Holzer and E. D. Siggia

FIG. 25. The left–right-averaged temperature-derivative PDF of Ref. 36. The temperature was measured at the center of a helium convection cell at Rayleigh number Ra$=7.3\times10^{10}$. The inset shows a blowup of the center of the PDF. The dotted line is a fit to the stretched exponential form, Eq. (17), with $(\alpha, \beta)=(0.347, 5.09)$.

by characteristic values of the gradient. A break in the distribution is expected for $|\nabla\theta| \sim \widetilde{\theta}\sqrt{s/\kappa}$, where s is the maximum sustained strain (on the order of the RMS), and $\widetilde{\theta}$ is a scalar difference, of at most $\mathcal{O}(gL)$, over the length $\sqrt{\kappa/s}$. This is clearly seen in Figs. 13 and 14, but the break falls too far in the tail to be visible for OU advection, where we estimate the crossover point by $\sim 6.8(Lk_{max}/\pi)^{1/3}$ using the RMS value of the strain and $\widetilde{\theta}\sim gL$. There is no change in any of the gradient PDFs at all for $|\nabla\theta|\sim\sigma$, which a priori was not obvious to us. Finally, there is the regime $|\nabla\theta| \lesssim g$, where the PDF is rounded in the case of OU advection (Fig. 4), whereas for restricted Euler advection on its natural time scale, it shows no break and continues into a cusp (Fig. 15). When the correlation time of the velocity is artificially decreased in the restricted Euler model, the center of the gradient PDFs becomes rounded (Figs. 22 and 24).[43]

Intermittency, in the sense that the scalar dissipation is either "on" or "off", is manifested in the gradient PDFs as much by the sharpness of their centers as by the flaring of their tails. If there are large regions with uniform $\Theta=\theta$ $+\mathbf{g}\cdot\mathbf{x}$, then they must be interleaved with cliffs to maintain the mean gradient. The statistically stationary state of our models, maintained by the mean scalar gradient, was essential to bring this out. If one were to run random large-scale initial data forward several correlation times,[44] the gradient PDF would be rounded on a scale set by the variance of the initial distribution of gradients.

We see no clear evidence for a lognormal distribution for $\nabla\theta$ or the dissipation and, instead, fit both successfully to stretched exponentials. We do not feel that the published experimental fits[45] to lognormal behavior are definite nor

preclude a stretched-exponential form.[44] There is certainly a compelling argument for lognormal gradients when there is no dissipation and the dynamics is integrated for a fixed time.[28] However, this reasoning does not carry over to the statistically stationary case.[23]

Although both our models generate a ramp-and-cliff structure and a $\mathcal{O}(1)$ skewness as in experiments,[3–5,11,26] one must still inquire whether the mechanisms we have uncovered plausibly operate in real turbulence. In both models the cliffs organize approximately along instantaneous streamlines transverse to $\hat{\mathbf{g}}$ emanating from saddle points of the streamfunction, so one might suspect that we see some vestige of a static 2-D velocity. However, what is required is merely a mixing time shorter than the correlation time of the velocity, and in that respect recall that the mixing time is Reynolds independent within Kolmogorov theory.

It is encouraging that a similar correlation between the cliffs and a conditionally averaged velocity emerged from experiments with a planar jet.[26] The large-scale eddies, which are a well-known feature of two-dimensional free-shear flows, appear to be responsible for the converging flow which gives rise to the cliffs. It is noteworthy that we see the same mechanism at work for a simple Gaussian velocity field.

The OU model suffers from a lack of Galilean invariance (the small scales are not advected by the large scales), so that saddle points, where $\mathbf{v}=0$, and the separatrices connecting them, are indeed singled out. In the OU model, a Galilean transformation cannot be accomplished by simply shifting the large-scale velocity by a constant velocity, $\mathbf{v}_0$. Because the model does not generate a corresponding coordinate transformation, $\mathbf{x}\rightarrow\mathbf{x}+\mathbf{v}_0 t$, for the velocity field itself, adding $\mathbf{v}_0$ merely creates bands of open streamlines which erode the ramps and broaden the cliffs. Nevertheless, the OU model is not obviously a pathological representation of real turbulence in the appropriate frame, where $\langle\mathbf{v}\rangle=0$. A more quantitative theory than what we have at present is needed to make any precise connections between the OU model and real turbulence, and to explain at a more fundamental level the sharpness of the cliffs and their $\mathcal{O}(gL)$ height.

The restricted Euler model (16) has reasonable invariance properties and is a physically sensible realization of the small-Pr limit in 2D. Although a trend toward a k^{-1} spectrum can be seen in Fig. 12, for the Pe studied with physical dissipation, numerical factors suppress a k^{-1} spectrum and lead to a $\mathcal{O}(1)$ skewness with gradient PDFs which are sharply peaked on the scale of g. With increasing Pe, however, as the mixing time becomes much longer than the integral time, T, we expect Batchelor scaling to develop, the skewness to scale asymptotically as $\text{Pe}^{-1/2}$, and the gradient PDFs to become rounded on the scale of g. When high Pe is simulated via the use of a k^4 hyperdiffusivity, a k^{-1} spectrum indeed develops, the skewness decreases, and the center of the gradient PDFs rounds. In 3D, we expect a model analogous to the restricted Euler model to show similar effects[46] although the PDFs should

always be rounded on the scale of g since in 3D the scalar can never be confined by streamlines.

Note added in proof. Recently Tong and Warhaft[47] have measured a scalar derivative skewness in grid turbulence comparable to the present work. Full 3-D numerical simulations of Pumir[48] also accord well with our results.

ACKNOWLEDGMENTS

[1] See, e.g., L. D. Landau and E. M. Lifshitz, *Fluid Mechanics*, 2nd ed. (Pergamon, New York, 1987).

[2] See, e.g., H. Tennekes and J. L. Lumley, *A First Course in Turbulence* (MIT Press, Cambridge, MA, 1972); original literature: A. M. Oboukhov, "Structure of the temperature field in turbulent flows," Izv. Akad. Nauk SSSR, Geogr. Geophys. Ser. **13**, 58 (1949); S. Corrsin, "On the spectrum of isotropic temperature fluctuations in isotropic turbulence," J. Appl. Phys. **22**, 469 (1951).

[3] P. G. Mestayer, C. H. Gibson, M. F. Coantic, and A. S. Patel, "Local anisotropy in heated and cooled turbulent boundary layers," Phys. Fluids **19**, 1279 (1976).

[4] C. H. Gibson, C. A. Friehe, and S. O. McConnell, "Structure of sheared turbulent fields," Phys. Fluids **20**, S156 (1977).

[5] P. G. Mestayer, "Local isotropy and anisotropy in a high-Reynolds-number turbulent boundary layer," J. Fluid Mech. **125**, 475 (1982).

[6] D. R. Dowling and P. E. Dimotakis, "Similarity of the concentration field of gas-phase turbulent jets," J. Fluid Mech. **218**, 109 (1990).

[7] W. J. A. Dahm, K. B. Southerland, and K. A. Buch, "Direct, high resolution, four-dimensional measurements of the fine-scale structure of $Sc \gg 1$ molecular mixing in turbulent flows," Phys. Fluids A **3**, 1115 (1991).

[8] P. L. Miller, "Mixing in high Schmidt number turbulent jets," Ph.D. thesis, California Institute of Technology, Pasadena, CA, 1991.

[9] Jayesh and Z. Warhaft, "Probability distribution of a passive scalar in grid-generated turbulence," Phys. Rev. Lett. **67**, 3503 (1991); "Probability distribution, conditional dissipation, and transport of passive temperature fluctuations in grid-generated turbulence," Phys. Fluids A **4**, 2292 (1992).

[10] J. Gollub, J. Clarke, M. Gharib, B. Lane, and O. Mesquita, "Fluctuations and transport in a stirred fluid with a mean gradient," Phys. Rev. Lett. **67**, 3507 (1991).

[11] K. R. Sreenivasan, "On local isotropy of passive scalars in turbulent shear flows," Proc. R. Soc. London Ser. A **434**, 165 (1991).

[12] Jayesh, C. Tong, and Z. Warhaft, "On temperature spectra in grid turbulence," Phys. Fluids **6**, 306 (1994).

[13] R. H. Kraichnan, "Small-scale structure of a scalar field convected by turbulence," Phys. Fluids **11**, 945 (1968).

[14] D. R. Dowling, "The estimated scalar dissipation rate in gas-phase turbulent jets," Phys. Fluids A **3**, 2229 (1991).

[15] F. N. Frenkiel and P. S. Klebanoff, "Two-dimensional probability distribution in a turbulent field," Phys. Fluids **8**, 2291 (1965).

[16] C. W. Van Atta and W. Y. Chen, "Correlation measurements in grid turbulence using digital harmonic analysis," J. Fluid Mech. **34**, 497 (1968).

[17] T. von Kármán and L. Howarth, "On the statistical theory of isotropic turbulence," Proc. R. Soc. London Ser. A **164**, 192 (1938).

[18] Equation (7) follows from balancing advection with dissipation in Eq. (2), squaring both sides, and averaging.

[19] G. K. Batchelor, I. D. Howells, and A. A. Townsend, "Small-scale variation of convected quantities like temperature in turbulent fluid. Part 2. The case of large conductivity," J. Fluid Mech. **5**, 134 (1959).

[20] G. K. Batchelor, "Small-scale variation of convected quantities like temperature in turbulent fluid. Part 1. General discussion and the case of small conductivity," J. Fluid Mech. **5**, 113 (1959).

[21] A. Pumir, B. Shraiman, and E. Siggia, "Exponential tails and random advection," Phys. Rev. Lett. **66**, 2984 (1991).

[22] M. Holzer and A. Pumir, "Simple models of non-Gaussian statistics for a turbulently advected passive scalar," Phys. Rev. E **47**, 202 (1993).

[23] B. I. Shraiman and E. D. Siggia, "Lagrangian path integrals and fluctuations in random flows," to appear in Phys. Rev. E.

[24] O. Métais and M. Lesieur, "Spectral large-eddy simulations of isotropic and stably stratified turbulence," J. Fluid Mech. **239**, 157 (1992).

[25] S. T. Thoroddsen and C. W. Van Atta, "Exponential tails and skewness of density-gradient probability density functions in stably stratified turbulence," J. Fluid Mech. **244**, 547 (1992).

[26] R. A. Antonia, A. J. Chambers, D. Britz, and L. W. B. Browne, "Organized structures in a turbulent plane jet: Topology and contribution to momentum and heat transport," J. Fluid Mech. **172**, 211 (1986).

[27] The estimation of the scalar derivative skewness and anisotropy is more straightforward than for the velocity, where a skewness is required to transfer energy, and a small anisotropy in $\langle (\partial_i v_i)^2 \rangle$ (no sum on i) can be maintained by the pressure. [P. K. Yeung and J. G. Brasseur, "The response of isotropic turbulence to isotropic and anisotropic forcing at the large scales," Phys. Fluids A **3**, 884 (1991). Also, J. Lumley, "Some comments on turbulence," Phys. Fluids A **4**, 203 (1992).] One might think that for real flows, the nonzero $\langle (\partial_i v_i)^3 \rangle$ could induce a significant scalar derivative skewness since $\nabla(\hat{g} \cdot v)$ is the source term for scalar gradients in Eq. (2). Formally solving (2) for its gradient by means of a suitable Lagrangian history Green function G, one obtains $\hat{g} \cdot \nabla \theta = \int G \hat{g} \cdot \nabla(\hat{g} \cdot v) dt\, dr$. Taking third moments, the velocity term is estimated on dimensional grounds as $\sim \tau_v^3 \langle (\partial_i v_i)^3 \rangle$, where τ_v is the velocity gradient correlation time on the dissipation scale. Since this expression is order unity, we obtain again a skewness which goes like $\sim Pe^{-3/2}$.

[28] R. H. Kraichnan, "Convection of a passive scalar by a quasi-uniform random straining field," J. Fluid Mech. **64**, 737 (1974).

[29] See, e.g., W. Horsthemke and R. Lefever, *Noise-Induced Transitions. Theory and Applications in Physics, Chemistry, and Biology* (Springer, New York, 1984), p. 49.

[30] See, e.g., Tennekes and Lumley (Ref. 2); original literature: G. I. Taylor, "Diffusion by continuous movements," Proc. London Math. Soc. Ser. 2 **20**, 196 (1921).

[31] R. H. Kraichnan and D. Montgomery, "Two-dimensional turbulence," Rep. Prog. Phys. **43**, 35 (1980).

[32] See, e.g., R. H. Kraichnan, "Inertial ranges in two-dimensional turbulence," Phys. Fluids **10**, 1417 (1967).

[33] G. S. Patterson and S. A. Orszag, "Spectral calculations of isotropic turbulence: Efficient removal of aliasing interactions," Phys. Fluids **14**, 2538 (1971).

[34] Under these conditions, the OU model, when run for many integral times on a 64^2 lattice, does not in fact produce exponential tails. Although the Pe is necessarily low then, the absence of exponential tails may in part be due to the independence of the velocity modes in the OU model. In the path-integral approach of Ref. 23, exponential tails result from paths along which the large-scale strain is suppressed. In the OU model, contrary to real turbulence, the small-scale strain is independent and not controlled by the large-scale strain. When we use the OU model with its velocity restricted to a band of wave numbers, the scalar PDF has exponential tails as for restricted Euler advection.

[35] The sampling times of the Pe=627 and 1.54×10^3 PDFs shown in Figs. 2–4 were less than the total sampling time, t_r, used for calculation of the moments of Tables I and III. The Pe=627 and 1.54×10^3 curves were obtained by sampling over $47.7T$ and $19.1T$, respectively.

[36] E. S. C. Ching, "Probabilities for temperature differences in Rayleigh–Bénard convection," Phys. Rev. A **44**, 3622 (1991); (private communication).

[37] B. J. Gluckman, H. Willaime, and J. P. Gollub, "Geometry of isothermal and isoconcentration surfaces in thermal turbulence," Phys. Fluids A **5**, 647 (1993).

[38] The negative peaks scaled rather better, but with $Pe^{3/4}$. This may well be a coincidence; *a priori*, it is certainly not expected since the Oboukhov-

1836   Phys. Fluids, Vol. 6, No. 5, May 1994

M. Holzer and E. D. Siggia

Corrsin scale[2] refers directly to a wave number and not to any characteristic value of $\nabla\theta$.

[39] As for all runs with the restricted Euler model, we verified numerically that the one-point velocity PDF is Gaussian (even with only ten modes).

[40] P. B. Phines and W. R. Young, "How rapidly is a passive scalar mixed within closed streamlines?," J. Fluid Mech. **133**, 133 (1983). See also, N. O. Weiss, "The expulsion of magnetic flux by eddies," Proc. R. Soc. London Ser. A **293**, 310 (1966).

[41] M. N. Rosenbluth, H. L. Berk, I. Doxas, and W. Horton, "Effective diffusion in laminar convective flows," Phys. Fluids **30**, 2636 (1987). Also, B. I. Shraiman, "Diffusive transport in a Rayleigh–Bénard convection cell," Phys. Rev. A **36**, 261 (1987).

[42] B. Castaing, G. Gunaratne, F. Heslot, L. Kadanoff, A. Libchaber, S. Thomae, X.-Z. Wu, S. Zaleski, and G. Zanetti, "Scaling of hard thermal turbulence in Rayleigh–Bénard convection," J. Fluid Mech. **204**, 1 (1989).

[43] When we artificially increase the velocity correlation time by the same device, the cusp of the gradient PDFs sharpens yet further.

[44] A. R. Kerstein and W. T. Ashurst, "Lognormality of gradients of diffusive scalars in homogeneous two-dimensional mixing systems," Phys. Fluids A **27**, 2819 (1984).

[45] W. J. A. Dahm and K. A. Buch, "Lognormality of the scalar dissipation pdf in turbulent flows," Phys. Fluids A **1**, 1290 (1989).

[46] A. Pumir (private communication, 1993).

[47] C. Tong and Z. Warhaft, "On passive scalar derivative statistics in grid turbulence," to appear in Phys. Fluids (1994).

[48] A. Pumir, "A numerical study of the mixing of a passive scalar in three dimensions in the presence of a mean gradient," to appear in Phys. Fluids (1994).